THE BELL SYSTEM TECHNICAL JOURNAL

DEVOTED TO THE SCIENTIFIC AND ENGINEERING ASPECTS OF ELECTRICAL COMMUNICATION

Volume 55 November 1976 Number 9

An Optical Apparatus for Very-Small-Angle Light Scattering—Design, Analysis and Performance

By J. B. LASTOVKA

(Manuscript received April 4, 1976)

We describe an optical apparatus designed and built to extend conventional light-scattering measurements to the very-small-angle regime. The present instrument covers the angular range $0.003° \leqq \theta \leqq 0.15°$ with an instrumental resolution (HWHM) of $0.00045°$ (1.6 arc seconds), and exhibits an exceptionally low stray-light background. The theoretical and practical considerations important in achieving this performance are analyzed in detail. Besides its primary purpose of studying long-wavelength (0.01 cm to 1 cm) thermally driven fluctuations, the present type of apparatus should also prove quite useful in other areas where long-wavelength perturbations must be probed, such as, (i) holographic and optical memory imaging, (ii) surface roughness testing, and (iii) index of refraction profiling.

I. INTRODUCTION

Laser light scattering has, over the past decade, been developed[1–3] into an extremely powerful tool for probing the long-wavelength ($\Lambda_f \approx 2 \times 10^{-5}$ cm to 2×10^{-3} cm) elementary excitations of liquids, gases, and solids. Combined with diffraction grating, Fabry-Perot, or optical mixing spectrometers the technique is capable of spanning an impressive range of more than 13 decades in energy or frequency measurement. Yet, in contrast to what has happened in the field of inelastic X-ray scattering,[4,5] very little has been done to utilize very-small-angle (VSA) light scattering to probe longer-wavelength ($\Lambda_f \approx 10^{-3}$ cm to 1 cm) excitations. With a few notable exceptions,[6–11]

most light-scattering experiments have been limited to the scattering-angle range $\theta > 1°$.

There have been a number of reasons for this apparent lack of progress in the very-small-angle scattering regime. On the one hand, experimentalists in the field, encountering a seemingly divergent stray-light level at small angles, have assumed that attempts to work in the VSA region would present insurmountable problems. On the other hand, there did not appear to be any physical phenomena where the important elementary excitations were confined to the corresponding longer-wavelength regime. Or, in cases where they were, it seemed that the use of more conventional macroscopic experimental techniques represented a satisfactory experimental approach.

Recently, however, there has been a resurgent interest in problems involving general hydrodynamic instabilities[12] both in normal liquids and liquid crystals.[13–26] The "critical wavelengths" involved in the onset of these instabilities are, in general, controlled by some macroscopic dimension of the sample chamber and tend to fall in the range $100\ \mu\text{m} < \Lambda_c < 1$ cm. Light scattering is the only technique offering the possibility of probing these wavelengths without physically disturbing the sample and with a sensitivity sufficient to detect the thermally driven critical fluctuations. However, probing the excitation wavelength region $100\ \mu\text{m} < \Lambda < 1$ cm requires the capability of resolving and detecting the scattered light at very small angles, $0.3° \geqq \theta \geqq 0.003°$.

This paper describes the experimental progress which has been made in extending the light-scattering technique to this very-small-angle, long-wavelength regime.

In Section II, we describe the physical configuration of a light-scattering apparatus that has been constructed for use in the VSA region. This section also summarizes the measured performance characteristics of the instrument in terms of angular resolution and stray light. Section III is a detailed presentation of the basic diffraction and aberration considerations that influence the design of a VSA light-scattering apparatus. Section IV outlines various empirical observations made during the course of construction of the present instrument, relating to the stray-light behavior of optical components at small angles.

II. AN APPARATUS FOR VERY-SMALL-ANGLE LIGHT SCATTERING

2.1 Introduction

In this section, we present a general description of the physical layout and performance of a light-scattering apparatus that has been constructed for the VSA regime. The theoretical background and practical considerations necessary to analyze the detailed characteristics of the instrument are deferred to Sections III and IV. Although

designed specifically for the study of the Bénard convective instability, this apparatus embodies solutions to most of the problems to be encountered in the general small-angle light-scattering experiment.

2.2 Performance goals

The following performance goals were established for the present instrument and evaluated at the various stages of construction and modification:

(*i*) The ability to make quantitative measurements of both the scattered intensity and the temporal intensity autocorrelation function for scattering angles ranging from a few mrad down to at least 50 μrad. (We will, in general, specify angular deflections in μrad; Table I lists conversion factors to other common units of angular measure.)

(*ii*) A stray-light level per coherence solid angle in the scattered field ($d\mathcal{P}_{sl}/d\Omega_{COH}$) that was less than 10^{-6} of the incident beam power.

(*iii*) An angular instrumental resolution of less than 15 μrad.

(*iv*) The capability of continuously scanning the instrument over a reasonable range in scattering angle without the need for realignment.

(*v*) The attainment of near-diffraction-limited performance using customary spherical optics of reasonable cost.

Taken individually, each of the above goals can be met or bettered by existing optical instruments. To cite just two examples, the 200-inch Mount Palomar telescope has a diffraction-limit angular resolution of about 0.1 μrad; and, in a typical $\theta = 90$ degrees light-scattering experiment, the desired stray-light level would be considered a straightforward achievement. Insofar as the angular range is concerned, we can easily show that the scattered light observed at these angles is contributed by plane-wave components of the refractive-index per-

Table I — Conversion factors between various common units of angular measure

	Deg	Rad	mrad	μrad	Arc Min.	Arc Sec
1 Deg	1	0.0174	17.45	17,453	60	3600
1 Rad	5.73	1	10^3	10^6	3438	2.06×10^5
1 mrad	0.0573	10^{-3}	1	10^3	3.438	206.3
1 μrad	5.73×10^{-5}	10^{-6}	10^{-3}	1	0.0034	0.2063
1 arc min.	1/60	2.91×10^{-4}	0.291	291	1	60
1 arc sec.	1/3600	4.85×10^{-6}	4.85×10^{-3}	4.848	1/60	1

turbations in the sample whose wavelengths, Λ, are given by the small-angle Bragg condition

$$\Lambda = \lambda_0/\theta, \tag{1}$$

where λ_0 is the incident-beam wavelength. Therefore, probing the scattering-angle range from 50 μrad to 3 mrad gives information about Fourier components of the refractive index having wavelengths between 1.0 cm and 0.016 cm, respectively. Here we can point out that this spatial-frequency region is routinely examined by common interferometric checking methods and holographic techniques.

The instrument described in this paper is unique in that it meets *all* of the performance criteria simultaneously. In being able to probe perturbations with wavelengths as long as 1.0 cm, it represents a 100-fold improvement on previous low-stray-light-level scattering instrumentation, while its small stray-light background gives it a 1000-fold sensitivity advantage over conventional interferometric and holographic equipment. On a per-unit-aperture-size basis, its ability to resolve closely spaced faint (10^{-6}) and strong (1) features is about 50 times better than the Mount Palomar telescope.

2.3 Optical components and physical configuration of the instrument

Figure 1 sketches the optical configuration of the most recent version of the apparatus designed to meet the performance criteria set out in the preceding paragraphs. For brevity, we refer to this particular optical system as the MK VI instrument.

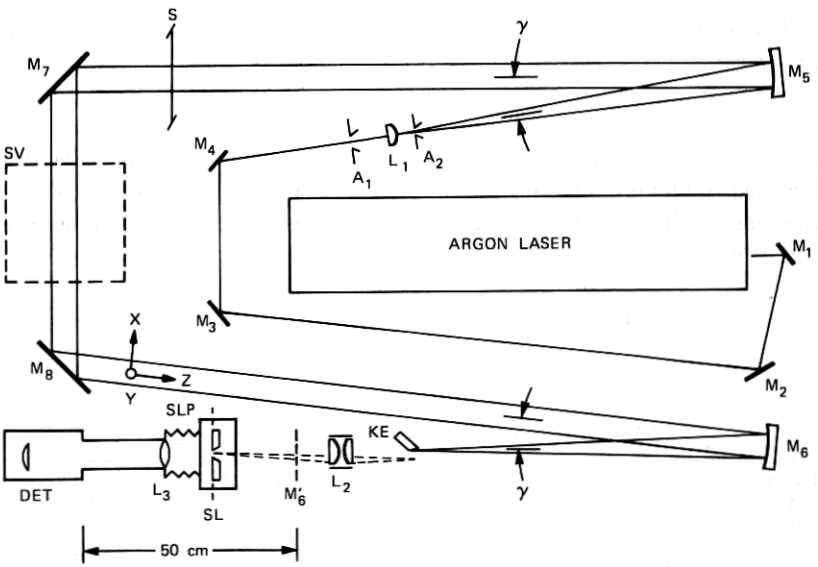

Fig. 1—Optical component layout of the MK VI small-angle-scattering instrument. Component sizes and spacings are shown approximately to scale.

Before discussing the specific function of the various elements of the spectrometer, we present below, for reference purposes, a brief description of each of these elements and their mounting following the identification scheme used in Fig. 1. Whenever spatial or angular displacements are specified, they are to be interpreted according to the conventions illustrated in Fig. 2. The $\hat{x}$ (or θ) and $\hat{y}$ (or φ) axes are taken to be mutually orthogonal cartesian (angular) coordinates perpendicular to the axial ray at the point in question. The $\hat{x}(\theta)$ direction will always lie in the plane of Fig. 1, the instrument's tangential plane, while $\hat{y}(\varphi)$ will denote the vertical or sagittal plane. The direction of beam travel defines the local $\hat{z}$ axis. The basic hardware components of the MK VI instrument are the following:

A_1—An adjustable circular diaphragm stop with an aperture diameter $d_{A1} \approx 5$ mm.

A_2—A fixed, precision-pinhole aperture, $d_{A2} = 100\ \mu$m. A_2 is mounted with $\hat{x}$ and $\hat{y}$ vernier adjustments relative to L_1.

Argon ion laser—The laser is normally adjusted to provide between 50 mW and 200 mW of output at either $\lambda_0 = 5145$ Å or $\lambda_0 = 5017$ Å. The laser used has a flat-long radius spherical resonator, placed at about $\frac{1}{4}$ hemispherical spacing, and oscillates in TEM_{00} modes only. The output is a well-collimated beam with a slight spheroidal distortion. The beam has a gaussian intensity profile with a diameter of 1.4 mm as measured to the $1/e^2$ points.

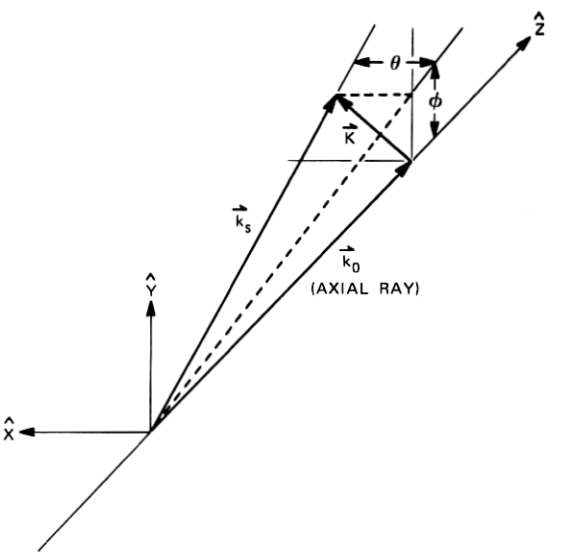

Fig. 2—Cartesian coordinate system for (x, y, z) showing the cartesian angular deflection θ and φ.

DET—A silicon-diode photodetector. The diode used is a photovoltaic device operated without bias as a current source. The detector has a 1-cm-diameter active area.

KE—A precision knife-edge custom-fabricated from neutral-density "black glass" plate. The 40-mm-long edge is straight to within 1 μm and nick free.

L_1—Plano convex achromat with a focal length $f_{L1} = 132$ mm. L_1 and A_2 share a common mount with vernier $\hat{y}$ and $\hat{z}$ degrees of freedom.

L_2—An anastigmatically mounted pair of plano convex achromats with an effective focal length $f_{L2} = 94.77$ mm. L_2 has $(\hat{x}, \hat{y}, \hat{z}, \hat{\theta}, \hat{\varphi})$ vernier adjustability.

L_3—An achromatic lens having $f_{L3} = 150$ mm and a mounted free aperture diameter of 35 mm.

M_1, M_2, M_3, M_4—Flat mirrors $1\frac{1}{2}$ inches in diameter with $\lambda/10$ surface figure.

M_5, M_6—Dielectrically coated, concave, spherical mirrors fabricated of fused quartz. They have a radius of curvature of 2 m and a surface conformity of $\lambda/10$. The mounted free aperture is 6.5 cm in diameter.

M_7, M_8—Aluminized, first-surface, fused-quartz, flat mirrors. They have a mounted free aperture of 13 cm and a surface figure of $\lambda/20$.

S—A bilateral slit with straight jaws that can be used to reduce the $\hat{y}$ dimension of the probe beam.

SL—A commercial, precision, bilateral slit. The jaws have a 50 mm usable height and an accurately adjustable opening range from 3 μm to 3 mm. The slit assembly is mounted on a precision x-z translational stage positioned by large-barrel micrometer heads with a maximum conforming error of about 1 μm. The $x(\theta)$-axis micrometer can be manually positioned or can be driven by a digitally controlled stepping motor.

SV—The location of the scattering sample.

These optical components are mounted on a 3-inch-thick aluminum slab that forms a stable base for the instrument. Because random laboratory air currents and temperature gradients can cause angular beam deflections comparable to the instrumental resolution, the entire apparatus is covered by an essentially air-tight Plexiglas* enclosure.

2.4 Functional description of the apparatus

We can most easily describe the basic optical characteristics of the instrument by following the beam path through the system starting at the laser source.

* Registered trademark of Rohn & Haas Company.

Mirrors M_1, M_2, M_3, and M_4 steer the laser output beam around to a spatial filter assembly comprised of A_1, L_1, and A_2. Lens L_1 and pinhole A_2 form the conventional spatial filter arrangement, while the pre-aperture A_1 serves to block high-angle-beam trash, such as multiple reflections in the laser resonator output mirror. The long path length through M_1–M_4 and aperture A_1 also provides a significant reduction in laser tube discharge light that would otherwise pass through the system.

The spherically spreading wave coming from A_2 is recollimated off-axis by M_5. The collimated beam leaving M_5 has a diameter* $D(1/e)$ of approximately 1.65 cm. The wave-front planarity of this beam is measured and adjusted using a wave-front shearing interferometer aligned to give a 7-mm shear in the tangential plane. The tangential direction wave-front curvature is reduced to less than $\lambda/8$ over the beam aperture by translating the spatial filter assembly along the laser beam ($\hat{z}$) axis. It is important to note that the use of this off-axis collimation scheme produces a large amount of astigmatism and tangential plane coma. As a result, *it is not possible to make the probe-beam wave fronts straight in both the $\hat{x}$ and $\hat{y}$ directions simultaneously.*† The alignment procedure just described is intended to give diffraction-limited angular resolution in the $\hat{\theta}$ plane with some sacrifice in $\hat{\varphi}$ direction resolution.

The collimated probe beam is now sent to the scattering object at SV via the flat mirror M_7. Flat mirror M_8 collects the transmitted beam and small-angle scattered light and directs them to M_6.

In the tangential focal plane of spherical mirror M_6, the directly transmitted beam is brought to a vertical ($\hat{y}$) line focus at a position we define as $x_{KE} \equiv 0$. Light that has been scattered by some angle θ is brought to line focus in the same plane, but at a displaced transverse position

$$x_{KE}(\theta) = f_{M6} \tan \theta \approx f_{M6}\theta, \tag{2}$$

where $f_{M6} = 100$ cm is the focal length of M_6. Therefore, for sufficiently small values of θ, where $\tan \theta \approx \theta$, angular deflection maps linearly into lateral displacement at the focus with a position-angle dispersion (PAD) constant given by

$$PAD(KE) = \frac{x_{KE}(\theta)}{\theta} = f_{M6} = 1\ \mu\text{m}/\mu\text{rad}. \tag{3}$$

The knife-edge KE is located in this tangential focal plane with its edge vertical and can be set to intercept the transmitted beam at

---

* See Section 3.1 for the definition of these quantities.
† See Section 3.2.

$\theta = 0$ to prevent it from entering the remaining portion of the optical system. In normal practice, KE is adjusted to occult all light for which $\theta \leqq 30$ to 50 μrad. The position and orientation of KE relative to M_6 is fixed with diffraction-limited accuracy using the standard Foucault knife-edge test procedure.

Lens pair L_2 re-images the focal plane of M_6 onto the vertically oriented main receiving slit SL with a magnification of about (2.54). Therefore, the dispersion constant in the slit plane has the value

$$PAD(SL) = 2.54\ \mu\text{m}/\mu\text{rad} \tag{4}$$

or

$$PAD(SL) = 0.0001\ \text{in.}/\mu\text{rad}. \tag{5}$$

The magnification by L_2 allows the scattering angle θ to be read directly on the "english-units" micrometer that positions the slit. More importantly, it relaxes the stability and accuracy requirements that must be imposed on the slit scan mechanism. Since SL has a minimum opening setting of roughly 3 μm, the slit-limited angular resolution is about 1 μrad.

The proper locations and orientations for the main slit SL and lens L_2 are determined by an iterative procedure in which one of the jaws of SL and the *image* of the knife-edge formed by L_2 at the slit plane are positioned to form an apparent two-jawed slit. The absence of distortion in the Fraunhofer diffraction pattern formed when this "slit" is illuminated by a collimated beam becomes a diffraction-limited test for correct lens and slit alignment.

The scattered light passed by the main slit is collected by L_3 and sent to the photodiode DET. The focal length and position of L_3 are chosen such that the real image of the limiting aperture of M_6 formed at the plane M_6' by lens L_2 is re-imaged onto the detectors active area.

2.5 Observed angular-resolution performance

We can assess the θ direction angular resolution of the MK VI apparatus from measurements of intensity as a function of slit position (x) in the absence of a scattering object. Two such "instrumental profiles" are shown in Fig. 3. The ordinate scale is logarithmic in the detector photocurrent with a rough correspondence of 200 μA/mW of optical power. Curves A and B were taken under identical conditions except for the position of the knife-edge KE. For curve A, the knife-edge was withdrawn to allow the direct probe beam to reach the scanning slit, while for curve B, it was positioned to occult all light in the region $\theta \gtrsim 50$ μrad. Note that the use of the knife-edge provides a significant decrease in observed stray-light level, the reduction amounting to about an order of magnitude improvement for $\theta \gtrsim 600$ μrad (see Section IV).

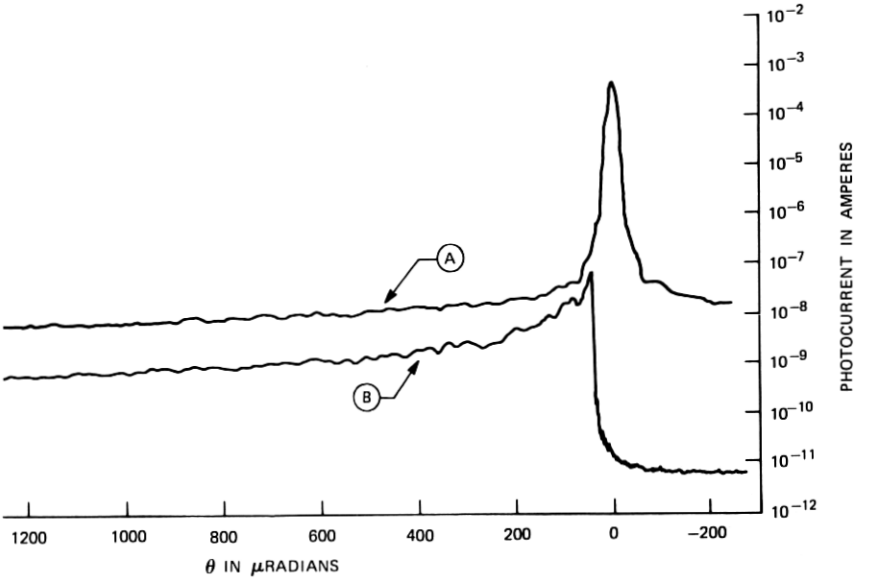

Fig. 3—Observed instrumental profiles for the MK VI apparatus plotted on a logarithmic intensity scale. Curve B was obtained with the knife-edge, *KE*, occulting the direct beam, while curve A was measured with *KE* retracted.

An expanded view of the $\theta \cong 0$ region of Fig. 3 is shown in Fig. 4. The dashed curve represents a best fit of the gaussian $\exp - [\theta^2/\delta\theta^2(1/e)]$ to the instrumental line shape, as detailed in Section 3.1. The full width at half-maximum of the fitted curve is

$$\Delta\theta(\tfrac{1}{2}) = 16\ \mu\text{rad}. \tag{6}$$

For the traces shown in Figs. 3 and 4, the main slit width was set at 5 μm which, from eq. (5), is equivalent to a 2-μrad acceptance angle. Under these conditions, the effect of artificial slit broadening on the line shape may be neglected, as outlined in Appendix A.

Deriving a value for the sagittal, or $\hat{\varphi}$ direction, resolution is a more complicated procedure because of the large instrumental astigmatism (see Section 3.2). However, a pragmatic number can be given using the following operational definition. If the *sagittal* resolution were measured in the *tangential* focal plane of M_6, the location of the main slit, the instrumental profile would have a full width at half maximum given by

$$\Delta\varphi(\tfrac{1}{2}) = 93\ \mu\text{rad}. \tag{7}$$

(See Section 3.2, especially Figs. 16 and 17.)

The overall angular resolution characteristics of the instrument are illustrated in Fig. 5. This sketch shows various fraction-of-maximum-intensity contours for the instrumental profile as determined at the main slit plane.

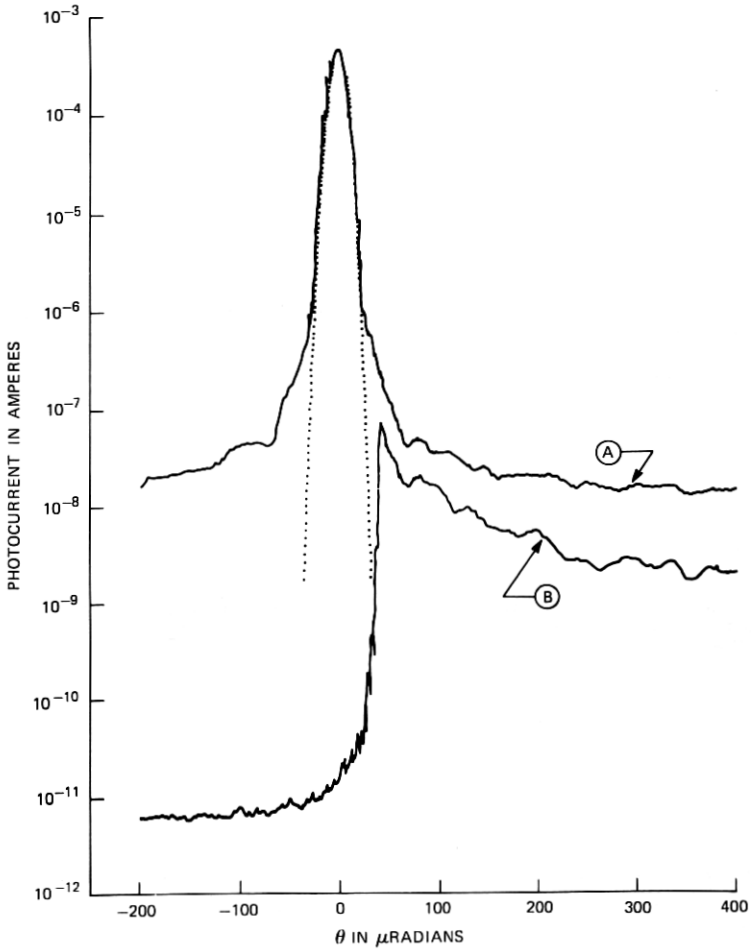

Fig. 4—Measured instrumental profiles for the MK VI apparatus in the region around $\theta = 0$. Curve B was obtained with the knife-edge, KE, occulting the direct beam, while curve A was measured with KE retracted. Dotted curve is best fit of the function $\exp[-\theta^2/\delta\theta^2(1/e)]$ to the transmitted beam profile.

The measured profiles presented in Figs. 3 and 4 and the corresponding contours of Fig. 5 were obtained using the full $\hat{y}$-axis beam height of the instrument, that is, in the absence of aperturing of the probe beam by slit S of Fig. 1. As such, the quoted $\Delta\varphi$ resolution does not include any diffraction broadening associated with $\hat{y}$ direction vignetting of the main beam. At full aperture, the instrument's θ resolution is essentially diffraction limited, while the φ resolution is dominated by astigmatic blurring. However, as the beam height is stopped down, diffraction spreading will eventually override the astigmatism and the instrument will be solely diffraction limited. For

the MK VI, this crossover point occurs at a beam height of about 0.5 cm or roughly $\frac{1}{10}$ of the full design aperture. Therefore, the most advantageous use can be made of the present apparatus when the desired probe-beam geometry consists of a collimated "sheet" or ribbon illumination.

2.6 *Analysis of stray-light performance*

A second crucial performance characteristic of any light-scattering instrument is its stray-light level in relation to the scattering efficiency of the sample under investigation. For the MK VI instrument, the ratio of recorded stray-light photocurrent to the photocurrent observed at the peak of the transmitted beam, say, can be read directly from Figs. 3b and 4b; however, this ratio is not of immediate physical

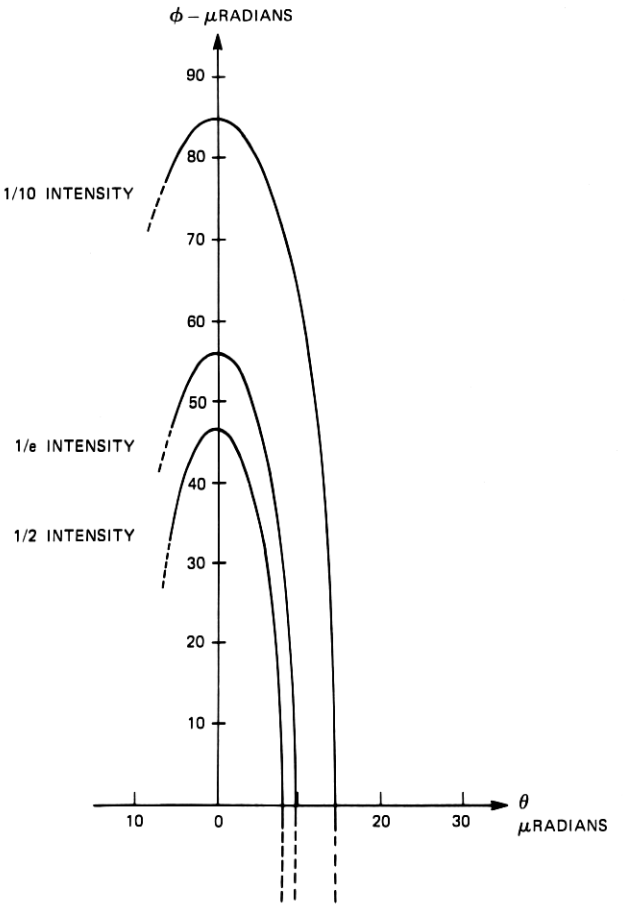

Fig. 5—Contours of constant intensity for the instrumental line shape. Each contour is labelled in terms of a fraction of the peak intensity, $I(\theta = 0, \varphi = 0)$.

significance because of the effects of residual instrumental astigmatism. The directly measured $i(\theta)/i(0)$ ratio requires a certain amount of mathematical interpretation to provide the stray-light ratio values that will be relevant in signal-to-noise or observability calculations.[1–3,27] In general, the quantities that are most important in this regard are:

(*i*) The scattered power per unit solid angle divided by the incident probe-beam power:

$$\frac{1}{\mathcal{P}_0}\frac{d\mathcal{P}_s(\theta,\ \varphi)}{d\theta d\varphi} \equiv \frac{d\mathcal{R}_s(\theta,\ \varphi)}{d\Omega}. \tag{8}$$

The ratio $[d\mathcal{R}_s(\theta,\ \varphi)/d\Omega]$ is a frequently used measure of the scattering power of an object; calculating a value of this ratio appropriate to the *stray* light $[d\mathcal{R}_{st}(\theta,\ \varphi)/d\Omega]$ provides a basis for estimating the observability of a particular scattering feature. This quantity can be extracted more or less directly from $i(\theta)/i(0)$ given (1) the effective solid angle subtended by the main slit and detection optics, and (2) the instrumental profile contours of Fig. 5.

(*ii*) The normalized scattered power per scattering normal mode:

$$\frac{\mathcal{P}_s(\mathbf{K}_j)}{\mathcal{P}_0}. \tag{9}$$

This latter quantity appears in scattered intensity calculations in which the index-of-refraction perturbations in the illuminated scattering volume are represented in terms of an orthonormal plane wave Fourier expansion.[3,27] The mean-square amplitude of these modes and their scattering efficiency are, in general, easily calculated from the known physical properties of the sample. Characterizing the stray-light via a ratio $\mathcal{P}_{st}(\mathbf{K}_j)/\mathcal{P}_0$ provides another convenient way of determining the observability of the scattering from a particular sample object.

(*iii*) The normalized scattered power per coherence solid angle in the scattered field:

$$\frac{1}{\mathcal{P}_0}\frac{d\mathcal{P}_s(\theta,\ \varphi)}{d\Omega_{COH}} = \frac{d\mathcal{R}_s(\theta,\ \varphi)}{d\Omega}\,\Omega_{COH}. \tag{10}$$

This quantity appears in signal-to-noise ratio calculations relevant to determining the spectrum of the scattered light from measurements of the temporal autocorrelation function or spectrum of the detected photocurrent.[2,3,27] In this case, it is useful to also characterize the stray-light level in terms of the quantity $[d\mathcal{R}_{st}(\theta,\ \varphi)/d\Omega_{COH}]$. The ratio $[d\mathcal{R}_s/d\Omega_{COH}]$ differs from that defined in eq. (8) in that the solid angle is specified as being the solid angle of spatial coherence in the scattered field, Ω_{COH}. The coherence solid angle is a measure of the range in θ and φ about some arbitrary reference direction $(\theta,\ \varphi)$ over which the amplitude and/or phase of the scattered electric field exhibits statistically correlated behavior. In the typical light-scattering experi-

ment, the extent of spatial coherence in the scattered field is controlled by the geometry of the scattering sample and wave diffraction. In a first approximation,[27] the coherence solid angle is just the diffraction solid angle of the scattering source; that is,

$$\Omega_{COH} = \Delta\theta_{COH} \times \Delta\varphi_{COH} \cong \left(\frac{\lambda}{b_\theta}\right)\left(\frac{\lambda}{b_\varphi}\right), \tag{11}$$

where b_θ and b_φ are extremal dimensions of the illuminated sample volume as viewed from a direction specified by (θ, φ). However, for the MK VI instrument, the extent of the spatial coherence is partly determined by residual aberration effects, and an evaluation of the ratio $[d\mathcal{R}_{st}(\theta, \varphi)/d\Omega_{COH}]$ requires a specific calculation of the spatial-coherence properties of the optical field at the main slit plane.

Obtaining expressions for the various stray-light ratios when aberrations are present requires a rather lengthy detailed analysis, as is carried out in Section 3.3. For our purposes here, we merely quote those results that lead to the numerical ratios appropriate to the MK VI instrument. In each case, the procedure is to treat the observed stray-light level *as if it originated from a fictitious "sample"* placed at the normal position of the scattering volume. After deriving the expressions that relate slit-plane intensity to a real sample's scattering cross section, expressed for example as $[d\mathcal{R}_s(\theta, \varphi)/d\Omega]$, we utilize these results in reverse fashion to calculate the effective cross section of our fictitious stray-light sample. Of course, these expressions derive from the main slit-plane imaging characteristics of the instrument; therefore, in succeeding paragraphs, whenever angles or solid angles are specified, they are to be interpreted as slit-plane coordinates or areas converted to angular units via eq. (5). Consider first the quantity

$$\begin{aligned}\frac{d\mathcal{R}_{st}(\theta, \varphi)}{d\Omega_{COH}} &= \frac{1}{\mathcal{P}_0}\frac{d\mathcal{P}_{st}(\theta, \varphi)}{d\theta\, d\varphi}\,\Omega_{COH} \\ &= \frac{1}{\mathcal{P}_0}\frac{d\mathcal{P}_{st}(\theta, \varphi)}{d\theta\, d\varphi}\,\overline{\Delta\theta}_{COH}\overline{\Delta\varphi}_{COH},\end{aligned} \tag{12}$$

where $\overline{\Delta\theta}_{COH}$ and $\overline{\Delta\varphi}_{COH}$ are the full-width coherence angles in the θ and φ directions. When the main-slit acceptance angles $\Delta\theta_{SL}$ and $\Delta\varphi_{SL}$ satisfy the inequalities

$$\begin{aligned}\Delta\theta_{SL} &\ll \overline{\Delta\theta}_{COH} = 24.1\ \mu\text{rad} \\ \Delta\varphi_{SL} &\gg \overline{\Delta\varphi}_{COH} = 140.4\ \mu\text{rad},\end{aligned} \tag{13}$$

as they do for the profiles of interest here, the right-hand side of eq. (12) can be expressed in terms of the measured photocurrent, $i(\theta)$, as

$$\frac{d\mathcal{R}_{st}(\theta, \varphi = 0)}{d\Omega_{COH}} = \frac{i(\theta)}{i(0)} \times \sqrt{2}\,\frac{\overline{\Delta\varphi}_{COH}}{\Delta\varphi_{SL}}, \tag{14}$$

where $i(0)$ is the photocurrent observed at the peak of the direct

transmitted beam. In writing eq. (14), we have assumed that $\Delta\varphi_{SL}$ is symmetrically placed around $\varphi = 0$. The ratio $[\Delta\varphi_{SL}/\Delta\varphi_{COH}]$ is essentially the number of slit-plane coherence areas sampled by the detection optics. For the instrumental profiles shown in Figs. (3) and (4), $\Delta\varphi_{SL}$ was limited solely by the free aperture of lens L_3. Using the proper lens free aperture diameter and the linear dispersion constant given in eq. (5), we find an effective slit-acceptance angle

$$\Delta\varphi_{SL} \cong 1.4 \times 10^4\ \mu\text{rad} = 0.79°.$$

This value of $\Delta\varphi_{SL}$ corresponds to a slit height that samples approximately 100 coherence areas. The ratio $[\Delta\varphi_{SL}/\Delta\varphi_{COH}]$, eq. (14), and the data of Fig. 3 combine to give the $[d\mathcal{R}_{st}(\theta, 0)/d\Omega_{COH}]$ values listed in Table II.

The normalized stray-light power per mode can be found from $[d\mathcal{R}_{st}(\theta, 0)/d\Omega_{COH}]$ by the methods detailed in Section 3.3. The basic procedure involves calculating both the scattered power per coherence area and $\mathcal{P}_s(\mathbf{K}_j)$ from a common starting point to obtain the correction term that relates them. In the present case, the required relationship has the form

$$\frac{d\mathcal{R}_{st}(\theta, 0)}{d\Omega_{COH}} = \frac{\mathcal{P}_{st}(\mathbf{K}_j)}{\mathcal{P}_0} \times \frac{\overline{\Delta\varphi_{COH}}}{(\lambda/b_y)} \frac{\overline{\Delta\theta_{COH}}}{(\lambda/b_x)}, \tag{15}$$

where b_x and b_y are the clear aperture width and height of the instrument and λ is the optical wavelength. The product of the ratios

$$\frac{\overline{\Delta\varphi_{COH}}}{(\lambda/b_y)} \quad \text{and} \quad \frac{\overline{\Delta\theta_{COH}}}{(\lambda/b_x)}$$

is a weighted measure of the number of $\mathbf{K}_j$ modes contributing to the power observed in a single coherence area at the main slit. At the full aperture of the MK VI instrument, $b_x = 5$ cm and $b_y = 5$ cm, the correction factor has the value

$$\frac{\overline{\Delta\varphi_{COH}}}{(\lambda/b_y)} \frac{\overline{\Delta\theta_{COH}}}{(\lambda/b_x)} = 33.6. \tag{16}$$

Table II — Numerical values of various stray-light ratios for the MK VI instrument at selected scattering angles

θ-μrad	$i(\theta)/i(0)$	$d\mathcal{R}_{st}(\theta, 0)/d\Omega_{COH}$	$\mathcal{P}_{st}(\mathbf{K}_j)/\mathcal{P}_0$
50	1.07×10^{-4}	1.5×10^{-6}	4.5×10^{-8}
100	2.82×10^{-5}	4.0×10^{-7}	1.2×10^{-8}
200	9.55×10^{-6}	1.4×10^{-7}	4.0×10^{-9}
500	2.82×10^{-6}	4.0×10^{-8}	1.2×10^{-9}
1000	1.62×10^{-6}	2.3×10^{-8}	6.8×10^{-10}

$\Delta\theta_{SL} = 2\ \mu$rad, $\Delta\varphi_{SL} = 14{,}000\ \mu$rad, $\Delta\theta_{COH} = 24.1\ \mu$rad, and $\Delta\varphi_{COH} = 140.4\ \mu$rad.

Combining eqs. (15) and (16) with the values of $[d\mathcal{R}_{st}(\theta, 0)/d\Omega_{COH}]$ already calculated gives the stray-light-per-mode ratios to be found in Table II.

The numerical values of the various stray-light ratios may be put into perspective by calculating the amplitude of some physical perturbations that would generate a scattered intensity equal to the observed stray-light level. Based on a theoretical analysis of the scattering problem, it may be shown that, for sufficiently small scattering angles, the actual three-dimensional scattering volume can be taken to be equivalent to a two-dimensional phase-object placed normal to the incoming probe beam.[28] In this two-dimensional phase-plate equivalent, the scattering disturbances appear in the form of a spatially varying phase thickness $\psi(x, y)$, which is the line integral of the instantaneous index of refraction encountered by a ray traversing the actual sample at the lateral position (x, y). If $n(x, y, z)$ is the local index of refraction in the actual three-dimensional scattering problem then $\psi(x, y)$ is given by

$$\psi(x, y) = \frac{2\pi}{\lambda_0} \int_0^{L_z} n(x, y, z)dz, \tag{17}$$

where L_z is the length of the illuminated volume along the direction of the incident beam. The phase perturbation $\psi(x, y)$ may be represented in terms of a two-dimensional plane-wave Fourier expansion

$$\psi(x, y) = \sum_{K_x} \sum_{K_y} \tilde{\psi}(\mathbf{K}_j) e^{iK_x x} e^{iK_y y}, \tag{18}$$

with the $\mathbf{K}_j = (K_x, K_y)$ chosen to make the expansion functions orthonormal over the instrument's full aperture. In this formulation of the problem, the normalized scattered power per $\mathbf{K}_j$ mode has the simple form

$$\frac{\mathcal{P}_s(\mathbf{K}_j)}{\mathcal{P}_0} = \tfrac{1}{4}\langle |\tilde{\psi}(\mathbf{K}_j)|^2 \rangle, \tag{19}$$

where the angular brackets denote an appropriate time or ensemble average.

The expression for the scattered power given in eq. (19) may be used to interpret the stray-light levels observed in the MK VI instrument in terms of a minimum detectable amplitude for a specific physical scattering mechanism. In succeeding paragraphs, we consider three such scattering processes: (*i*) static index of refraction modulation in a transparent slab, (*ii*) surface height modulation on a reflecting mirror, and (*iii*) temperature modulation in an otherwise homogeneous liquid.

2.6.1 Refractive modulation in a slab

The scattering from a static sinusoidal refractive-index modulation in a plate is an interesting model problem relevant to holographic

memories and general phase-grating problems. We take the sample object to be a nominally homogeneous plate of thickness L_z and refractive index n_0 in which a small sinusoidal index disturbance

$$\delta n(x, y, z) = \delta n e^{i\mathbf{Q}\cdot\mathbf{r}} \tag{20}$$

has been created. The index perturbation is assumed to be uniform in the $\hat{z}$ direction such that $\mathbf{Q}$ lies in the (x, y) plane. The local index in the plate is

$$n(x, y, z) = n_0\left[1 + \frac{\delta n}{n_0} e^{i\mathbf{Q}\cdot\mathbf{r}}\right] \tag{21}$$

which, when inserted in eq. (17), gives the phase function $\psi(x, y)$ as

$$\psi(x, y) = \frac{2\pi}{\lambda_0}\left[n_0 L_z + \delta n L_z e^{i\mathbf{Q}\cdot\mathbf{r}}\right]. \tag{22}$$

The required Fourier amplitude, $\langle|\tilde{\psi}(\mathbf{K}_j)|^2\rangle$, is obtained by inspection from eq. (22) as

$$\langle|\psi(Q)|^2\rangle = \left[\left(\frac{2\pi}{\lambda_0}\right)\left(\frac{\delta n}{n_0}\right) n_0 L_z\right]^2. \tag{23}$$

This result may be used together with eq. (19) to obtain the perturbation amplitude $(\delta n/n_0)$ necessary to produce a given scattered power per mode. For example, taking $L_z = 1$ cm, $n_0 = 1.5$, and $\lambda_0 = 5000$ Å, we find that a refractive-index amplitude $\delta n/n_0 = 1.2 \times 10^{-9}$ yields a normalized scattered power per mode equal to the MK VI's observed stray-light value at $\theta = 100$ μrad. To produce scattering at this angle, the wavelength of the perturbation $\Lambda = 2\pi/|\mathbf{Q}|$ would have to be $\Lambda = (\lambda_0/\theta) = 0.5$ cm. Table III lists the "background equivalent" $\delta n/n_0$ values corresponding to other values of $\theta(\Lambda)$.

2.6.2 Height modulation on a reflecting surface

Another interesting example from the viewpoint of stray-light level comparison is the scattering from a surface height disturbance on an otherwise perfect reflecting mirror. Clearly, this problem can also serve as a model for *calculating* the instrumental background when mirror surface roughness (see Section IV) is the dominant source of stray light.

Since the primary effect of a surface height deviation is to produce a phase perturbation on the reflected wave-front, the phase function $\psi(x, y)$ can be written down immediately as

$$\psi(x, y) = \frac{(2)(2\pi)}{\lambda_0} h(x, y), \tag{24}$$

where $h(x, y)$ gives the local physical height displacement from the nominally perfect geometric surface.

Table III — Amplitudes of three scattering perturbations necessary to scatter an amount of light equal to the instrument's stray-light level

θ (μrad)	Λ (cm)	$\mathcal{P}_s(\mathbf{K}_j)/\mathcal{P}_0$	Refractive Perturbation ($\delta n/n_0$)	Surface Corrugation (δh-Å)	Temperature Perturbation (δT-°C)
50	1.0	4.5×10^{-8}	2.2×10^{-9}	0.16	6.8×10^{-6}
100	0.5	1.2×10^{-8}	1.2×10^{-9}	0.084	3.5×10^{-6}
200	0.25	4.0×10^{-9}	6.7×10^{-10}	0.049	2.0×10^{-6}
500	0.1	1.2×10^{-9}	3.6×10^{-10}	0.027	1.1×10^{-6}
1000	0.05	6.8×10^{-10}	2.8×10^{-10}	0.021	8.4×10^{-7}

We will take $h(x, y)$ to be a small, static, sinusoidal corrugation

$$h(x, y) = \delta h \, e^{i\mathbf{Q}\cdot\mathbf{r}} \tag{25}$$

for which the phase function is just

$$\psi(x, y) = \frac{4\pi\delta h}{\lambda_0} e^{i\mathbf{Q}\cdot\mathbf{r}}. \tag{26}$$

The Fourier amplitude $\langle|\tilde{\psi}(\mathbf{K}_j)|^2\rangle$ follows trivially as

$$\langle|\tilde{\psi}(\mathbf{K}_j)|^2\rangle = \left[\frac{4\pi}{\lambda_0}\delta h\right]^2. \tag{27}$$

Combining eqs. (27) and (19) with the data of Table II gives the "background equivalent" surface corrugation amplitudes listed in Table III. Again, these are the surface amplitudes necessary to yield a normalized scattered power-per-mode equal to the MK VI's stray-light level. For example, when $\Lambda = 2\pi/|Q| = 0.5$ cm, the "background equivalent" corrugation has an amplitude of $\delta h = 0.084$ Å or, in the usual surface-figure parlance,

$$\delta h \cong \lambda/60{,}000.$$

2.6.3 Temperature modulation in a liquid

As a final example, we consider an otherwise homogeneous slab of liquid of thickness L_z on which is impressed a small sinusoidal temperature disturbance,

$$\delta T(x, y, z) = \delta T e^{i\mathbf{Q}\cdot\mathbf{r}}, \tag{28}$$

with $\mathbf{Q}$ lying in the (x, y) plane. The calculation of the scattering from such an object is really just a simple extension of the result obtained above for refractive index modulation. The temperature perturbation produces an associated index disturbance that is responsible for the scattering. If the temperature perturbation in eq. (28) is impressed

isobarically, the associated index modulation is simply

$$\delta n(x, y, z) = \left(\frac{\partial n}{\partial T}\right)_P \delta T(x, y, z)$$
$$= \left(\frac{\partial n}{\partial T}\right)_P \delta T e^{i\mathbf{Q}\cdot\mathbf{r}}. \tag{29}$$

Equations (20) through (23) may now be used to obtain the relevant mean-square phase amplitude, namely,

$$\langle |\psi(\mathbf{Q})|^2 \rangle = \left[\frac{2\pi}{\lambda_0}\left(\frac{\partial n}{\partial T}\right)_P L_z \, \delta T\right]^2. \tag{30}$$

Taking $L_z = 1$ cm and $\lambda_0 = 5000$ A and using a typical value for $(\partial n/\partial T)_P$ in liquids, $(\partial n/\partial T)_P = -5 \times 10^{-4}/°C$, we find the background-equivalent temperature amplitudes listed in Table III.

2.7 Conclusion

In this section, we described the basic features of an optical instrument capable of extending conventional light-scattering measurements to an angular range (50 μrad to 3 mrad) not previously accessible. In addition to a diffraction-limited angular resolution of a few seconds of arc, the MK VI instrument exhibits an exceptionally low stray-light background making it an effective tool for probing small-amplitude-scattering processes. Besides its primary purpose of studying long-wavelength (0.01 cm to 1 cm) thermal fluctuations, the present type of apparatus should prove quite useful in other areas where long-wavelength perturbations must be probed, such as,

(*i*) Holographic and optical memory imaging.
(*ii*) Surface roughness testing.
(*iii*) Index of refraction profiling.

In general, the MK VI offers a sensitivity improvement of a factor of about 1000 over the instrumentation normally used for such measurements.

While we have given a rather broad overview of the apparatus in the present section, we have not attempted to present the fundamental considerations on which the design is based. We refer the reader who is interested in these questions to the remaining sections of this paper.

III. THEORETICAL CONSIDERATIONS IN THE DESIGN OF A VERY-SMALL-ANGLE LIGHT-SCATTERING APPARATUS

3.1 Aperture apodization

In the simplest analysis, the ultimate angular resolution of any optical instrument is limited solely by diffraction. The expression most

widely used to estimate the limiting resolution is the so-called Rayleigh criterion,[29]

$$(\Delta\theta)(\Delta d) \cong \lambda_0. \tag{31}$$

The quantities $\Delta\theta$ and Δd can be interpreted in two ways:

(*i*) If Δd is the diameter of a "collimated" beam, then $\Delta\theta$ is the actual angular spread of the beam imposed by diffraction.

(*ii*) If $\Delta\theta$ is the collection angle for light emanating from an object, then Δd is the smallest spatial detail that can be resolved on that object.

Neglecting for the moment the off-axis features of the actual MK VI instrument, we can duplicate its basic function with the two-lens system sketched in Fig. 6. Applying the Rayleigh criterion to this particular optical arrangement for a collimated beam diameter $b = \Delta d = 5$ cm, and with $\lambda_0 = 5000$ Å, predicts an instrumental angular spread

$$\Delta\theta_{\text{RAYLEIGH}} = 10\ \mu\text{rad}. \tag{32}$$

Unfortunately, taken by itself, this value for $\Delta\theta_{\text{RAYLEIGH}}$ contributes little in the way of a quantitative understanding of the instrument's small-angle performance. In fact, the Rayleigh criterion can be misleading in a number of ways. First, it does not indicate how much light an object would have to scatter to be "visible" when the scattering angle approaches $\Delta\theta_{\text{RAYLEIGH}}$. Second, it implies that the angular diffraction spread can be decreased to an arbitrarily small value by simply increasing the beam diameter $b = \Delta d$. In reality, the presence of unavoidable optical aberrations will always limit the attainable angular resolution. In designing an instrument which is to attain a resolution approaching the diffraction limit, a quantitative approach to the problem is mandatory.

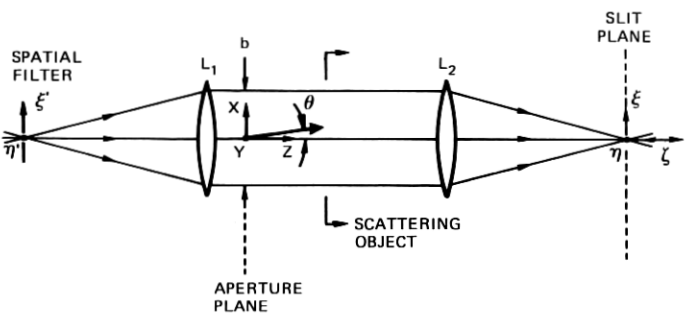

Fig. 6—A simplified "lens equivalent" version of the MK VI optical system.

An exact expression for the diffraction-limit resolution characteristics of an optical system may be obtained as follows. Let us assume we know the spatial dependence of the incident beam intensity on some surface in the optical system, say the aperture plane of Fig. 6. In our case, the electric field on this surface is of the form

$$E_0(x, y)e^{i(k_0 z_0 - \omega_0 t)}. \tag{33}$$

This aperture plane field can be decomposed into a set of infinitely extended plane waves,

$$E_D(\theta, \varphi) = E_D^0(\theta, \varphi)e^{-i(\mathbf{Q}\cdot\mathbf{r} - \omega_0 t)}, \tag{34}$$

propagating toward L_2 at various angles with respect to the $\hat{z}$ axis.* The plane-wave amplitudes, $E_D^0(\theta, \varphi)$, are found from the Fourier integral

$$E_D^0(\theta, \varphi) = \frac{1}{\lambda_0}\int\int_S dxdyE_0(x, y)e^{i(Q_x x + Q_y y)} \tag{35}$$

together with the relations,

$$\begin{aligned} |\mathbf{Q}| &= k_0 = 2\pi/\lambda_0 \\ Q_x &= \mathbf{Q}\cdot\hat{x} = k_0 \sin\theta \cong k_0\theta \\ Q_y &= \mathbf{Q}\cdot\hat{y} = k_0 \sin\varphi \cong k_0\varphi. \end{aligned} \tag{36}$$

Equation (35) is just a slightly modified form of the usual scalar diffraction theory result which utilizes spherically spreading waves as basis functions.[30]

Assume for the moment that lens L_2 in Fig. 6 is infinitely large and free of aberrations. Then each of the plane waves, $E_D(\theta, \varphi)$, is brought to a point focus in the slit plane at a position

$$\begin{aligned} \xi &= f\tan\theta \cong f\theta \\ \eta &= f\tan\varphi \cong f\varphi, \end{aligned} \tag{37}$$

where f is the focal length of L_2, and the approximate signs hold for small angles. Combining (35), (36), and (37) gives the field in the slit plane as

$$E_0(\xi, \eta) = \frac{1}{f\lambda_0}\int\int_S E_0(x, y)e^{i(2\pi/f\lambda_0)(\xi x + \eta y)}dxdy. \tag{38}$$

As eq. (38) shows, the field at the slit plane and the field at the aperture plane are related as Fourier transform pairs. It should be evident that eq. (38) can also be applied "backwards" in Fig. 6 to relate $E_0(x, y)$ to the field at the spatial filter aperture, $E_0(\xi', \eta')$. We will

* The cartesian coordinate and angle notation follows that adopted in Section II.

refer to the field $E_0(x, y)$ or its intensity

$$I_0(x, y) = \tfrac{1}{2}\sqrt{\epsilon\epsilon_0/\mu_0}E_0(x, y)E_0^*(x, y)$$

as the illumination or aperture function. The slit-plane field $E_0(\xi, \eta)$ or its intensity, $I_0(\xi, \eta)$, is the corresponding instrumental profile.

The procedure of aperture apodizing may be described simply as follows. The basic problem is to find and implement an instrumental illumination function, such that both the function itself and its transform have minimum spatial extent. The goal in a loose sense is to optimize the angular resolution per unit aperture opening. Of course, one of the general properties of Fourier transform pairs is that the second moments or "widths" of the pair members have an approximate inverse relationship. The Rayleigh criterion, in fact, is a simplified statement of this property. Even within the confines of this inverse relationship, however, there is still wide latitude for aperture apodizing, i.e., shaping the instrumental profile to obtain particularly desirable angular or spatial characteristics. Although the Fourier transform relationship between the illumination function and the instrumental profile in coherently illuminated optical systems is well known,[31–33] aperture apodizing schemes are not often applied in optical instrument design. Apodizing schemes are, however, extensively employed in high-frequency and microwave antenna design,[34,35] where they are used to create antenna systems exhibiting an angular directivity pattern that satisfies a particular objective.

In designing an apparatus for very-small-angle light scattering, the principal objective is the ability to observe the weak scattered light in close angular proximity to the unscattered beam. The goal, then, is an instrumental profile that not only has small angular half-power points but, more importantly, continues down rapidly to the 10^{-5} to 10^{-6} level. The proper shaping of the illumination function, $E_0(x, y)$ is absolutely crucial in obtaining this desired "steep-skirt" behavior.

In treating the question of aperture apodization for the MK VI instrument, we consider the optical system in the simplified form shown in Fig. 6. Therefore, the calculated instrumental profiles that are obtained below represent the instrument's ideal, diffraction-limited performance in the absence of all aberrations. The ways in which the residual aberrations of the actual off-axis configuration modify these results are taken up in detail in Section 3.2.

Given the idealized geometry of Fig. 6, the process of evaluating various illumination function/instrumental profile combinations can be further simplified by the following considerations. First, most of the interesting illumination functions and, therefore, their Fourier

transforms can be factored to the form

$$\begin{aligned} E_0(x, y) &= E_0(x)E_0(y) \\ E_0(\xi, \eta) &= E_0(\xi)E_0(\eta). \end{aligned} \tag{39}$$

Second, in the MK VI apparatus, the open height of the main scanning slit guarantees that the measured slit-plane profile is the integral over all η of the slit-plane intensity $I_0(\xi, \eta)$. Under either of these circumstances, we need consider only a one-dimensional form of eq. (38), namely,

$$E_0(\xi) = \frac{1}{(f\lambda_0)^{\frac{1}{2}}} \int E_0(x) e^{i(2\pi/f\lambda_0)\xi x} dx, \tag{40}$$

where $\xi = f\theta$. The corresponding aperture and slit-plane intensities are

$$\begin{aligned} I_0(x) &= \frac{1}{2}\sqrt{\frac{\epsilon\epsilon_0}{\mu_0}}\, E_0(x)E_0^*(x) \\ I_0(\xi) &= \frac{1}{2}\sqrt{\frac{\epsilon\epsilon_0}{\mu_0}}\,\frac{1}{f\lambda_0}\left| \int E_0(x) e^{i(2\pi/f\lambda_0)\xi x} dx \right|^2. \end{aligned} \tag{41}$$

In presenting the results of calculations based on eq. (41), it is convenient to adopt a concise terminology to describe the spatial and angular widths of the functions involved. We use the following notation:

$D_x(\frac{1}{2})$—Full width at half-maximum intensity for $I_0(x)$
$d_x(\frac{1}{2})$—Half width at half-maximum intensity for $I_0(x)$
$D_\xi(\frac{1}{2})$—Full width at half-maximum intensity for $I_0(\xi)$ or $I_0(\xi')$
$d_\xi(\frac{1}{2})$—Half width at half-maximum intensity for $I_0(\xi)$ or $I_0(\xi')$
$\Delta\theta(\frac{1}{2})$—Full width at half-maximum intensity for $I_0(\xi)$ or $I_0(\xi')$, expressed as an angular equivalent via eq. (37), $\Delta\theta(\frac{1}{2}) = (1/f)D_\xi(\frac{1}{2})$
$\delta\theta(\frac{1}{2})$—Half width at half-maximum intensity for $I_0(\xi)$ or $I_0(\xi')$, expressed as an angular equivalent.

For arguments other than $(\frac{1}{2})$ these quantities, give the width at the specified fraction of the peak intensity. Since the absolute normalization of the various intensity functions depends only on the total beam power, we present all results in terms of the ratio quantities:

$$I_0(x)/I_0(0),\ I_0(\xi)/I_0(0),\ I_0(\theta)/I_0(0),$$

where $I_0(\theta)$ describes the slit-plane intensity with position ξ given in terms of the equivalent angular deflection $\theta = \xi/f$.

Figure 7 shows the instrumental profiles calculated for two interesting illumination functions. The first is the uniform field

$$E_0(x) = \begin{cases} E_0; & -b/2 \leqq x \leqq b/2 \\ 0; & \text{otherwise} \end{cases}$$

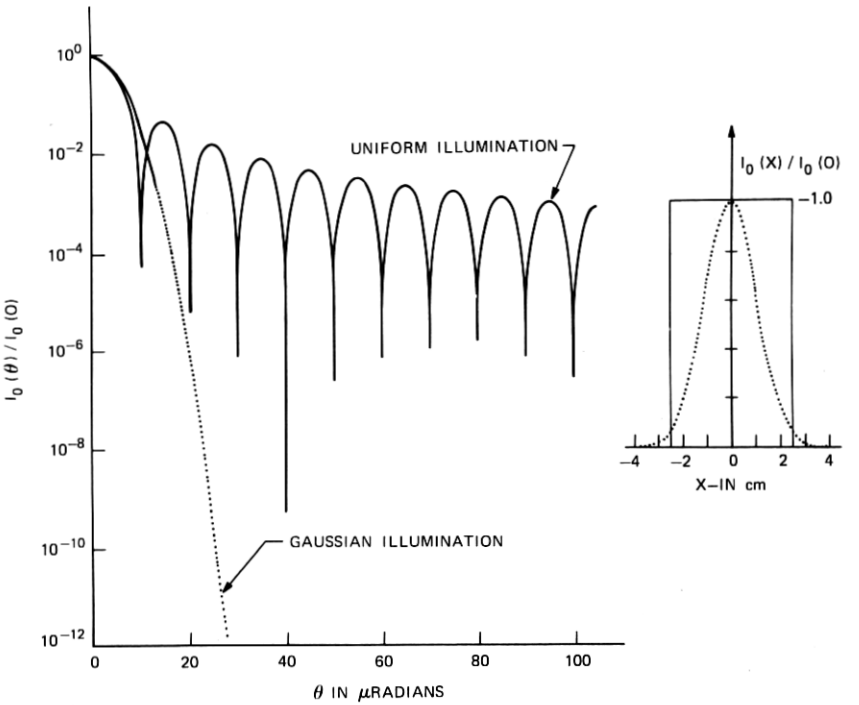

Fig. 7—Calculated instrumental profiles for uniform and gaussian illumination with $b = 5.0$ cm and σ chosen to give equal values of $\delta\theta(\frac{1}{2})$ for both profiles. The normalized illumination functions for each case are shown inset on a linear intensity scale.

for which one can easily calculate the following intensity ratios:

$$\begin{aligned} I_0(x)/I_0(0) &= \begin{cases} 1; & -b/2 \leqq x \leqq b/2 \\ 0; & \text{otherwise} \end{cases} \\ I_0(\xi)/I_0(0) &= \frac{\sin^2 (k_0 b\xi/2f)}{(k_0 b\xi/2f)^2} \\ I_0(\theta)/I_0(0) &= \frac{\sin^2 (k_0 b\theta/2)}{(k_0 b\theta/2)^2}, \end{aligned} \tag{42}$$

where $k_0 = (2\pi/\lambda_0)$. The second profile results from a gaussian aperture illumination,

$$E_0(x) = E_0\, e^{-x^2/2\sigma^2}$$

for which the relevant intensity ratios are

$$\begin{aligned} I_0(x)/I_0(0) &= \exp\,(-x^2/\sigma^2) \\ I_0(\xi)/I_0(0) &= \exp\,(-\sigma^2 k_0^2 \xi^2/f^2) \\ I_0(\theta)/I_0(0) &= \exp\,(-\sigma^2 k_0^2 \theta^2). \end{aligned} \tag{43}$$

The numerical parameters used in obtaining the curves plotted in Fig. 7 were

$$\lambda_0 = 5000 \text{ A}, \quad b = 5.0 \text{ cm}, \quad \sigma = 1.496 \text{ cm}. \tag{44}$$

The b value is representative of the maximum clear aperture of the MK VI apparatus; the value of σ was arbitrarily chosen to give equal $\delta\theta(\frac{1}{2})$ for both instrumental profiles. Also shown inset in Fig. 7 are the two aperture-plane intensity ratios, $I_0(x)/I_0(0)$. Note that the latter are plotted using a linear ordinate scale.

As is evident from these two calculated instrumental line shapes, the use of gaussian apodization is vastly superior to uniform illumination in regard to the observability of weak small-angle features even though the two $I_0(\theta)/I_0(0)$ profiles have identical half-widths. For example, at the 10^{-6} level we find

$$\delta\theta(10^{-6}) = 19.8\ \mu\text{rad} \quad \text{GAUSSIAN } I(x)$$
$$\delta\theta(10^{-6}) = 3183\ \mu\text{rad} \quad \text{UNIFORM } I(x).$$

In fact, from a theoretical standpoint, the gaussian is the ideal form of aperture functional. Among the families of possible illumination functions, it possesses a unique combination of two properties: (*i*) it has an extremely rapid shirt fall-off, and (*ii*) it goes over into itself under the Fourier transform operation. In a general situation where the available aperture illumination has some arbitrary (x, y) behavior, gaussian apodization would have to be accomplished by interposing a suitable neutral density mask at the aperture plane. Fortunately, laser sources with a reasonable cavity configuration and oscillating only on TEM_{00} modes have an output beam intensity pattern which is accurately gaussian, except in the extreme tails of the profile. The availability of such a source represents a crucial factor in the feasibility of constructing an instrument having the resolution and stray-light performance of the MK VI apparatus.

In the actual MK VI instrument, the ratio of the focal length of lens L_1 to that of mirror M_5 was chosen to generate a gaussian illumination function with an effective width

$$\sigma^* = d_x(1/e) = 0.826 \text{ cm} \tag{45}$$

in the collimated beam portion of the apparatus (see Fig. 1). The instrumental profile calculated via eq. (41) for this value of σ is plotted in Fig. 8. Also shown for comparison purposes is the profile to be expected if we uniformly illuminated the instrument's maximum design aperture

$$b^* = 5.0 \text{ cm}.$$

It is clear that for these specific values of σ and b, gaussian apodizing no longer exhibits an absolute superiority over uniform illumination. Although the "gaussian" profile still reaches the 10^{-6} level much more rapidly, it does sacrifice resolving power to the "uniform" profile down to approximately the 10^{-2} level. What this means to VSA scattering performance is the following. The "gaussian" instrument will excel in its ability to detect small amounts of light at very small scattering angles; however, it will not resolve approximately equal intensity features with as much detail as would the "uniform" instrument. As we see in the following paragraphs, the tradeoff, roughly speaking, involves paying for small-angle weak-intensity performance by sacrificing some ability to resolve the angular dependent features of the scattered light. This comparison can be made more quantitative by reference to Table IV, which gives various half-width angles for the profiles of Fig. 8.

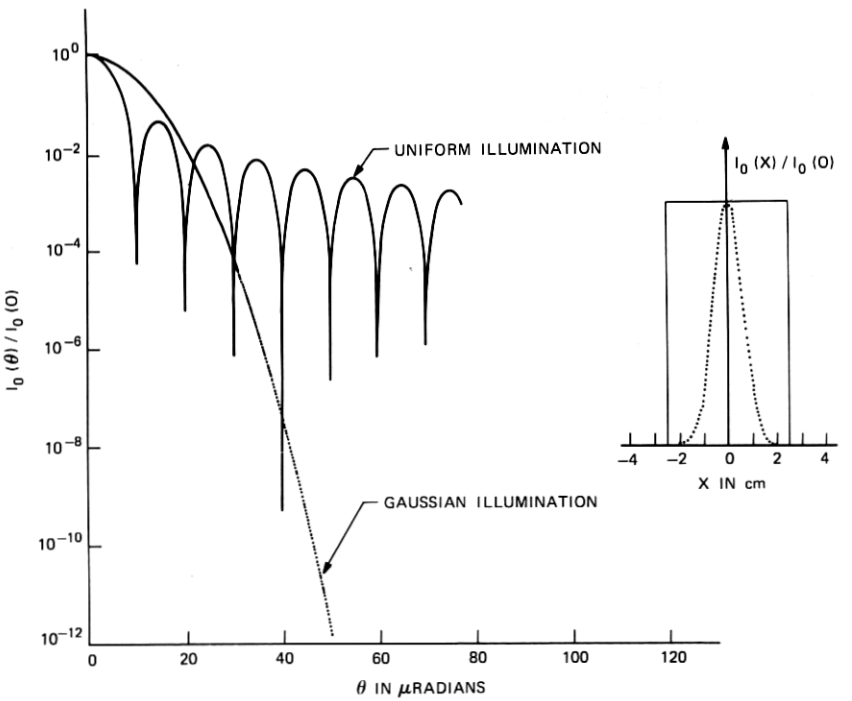

Fig. 8—Calculated instrumental profiles for uniform and gaussian illumination with $b = 5.0$ cm and $\sigma = 0.826$ cm. The b value corresponds to the maximum clear aperture of the MK VI instrument, while the σ value corresponds to the width of the gaussian illumination actually used in the present apparatus. Normalized illumination functions for each case are shown inset on a linear intensity scale.

Table IV—Calculated instrumental profile half-widths at various fractions of peak intensity for three different illumination functions

$\lambda_0 = 5000$ Å	Gaussian Illumination $d_x(1/e) = \sigma^*$ $\sigma^* = 0.826$ cm (μrad)	Uniform Illumination $d_x(1/e) = b^*/2$ $b^* = 5.0$ cm (μrad)	Truncated Gaussian Illumination $b = b^*$ $\sigma = \sigma^*$ $b/\sigma = 6.05$ (μrad)
$\delta\theta(1/2)$	8.0	4.43	8.09
$\delta\theta(1/e)$	9.6	5.23	9.69
$\delta\theta(10^{-1})$	14.6	7.36	14.62
$\delta\theta(10^{-2})$	20.7	31.8	20.6
$\delta\theta(10^{-3})$	25.3	100.6	25.5
$\delta\theta(10^{-4})$	29.2	318	29.7
$\delta\theta(10^{-5})$	32.7	1006	32.6
$\delta\theta(10^{-6})$	35.8	3183	76.8
$\delta\theta(10^{-7})$	38.7	10,060	243
$\delta\theta(10^{-8})$	41.3	31,830	768

From the inset plots of $I(x)/I(0)$ shown in Fig. 8, it may seem that the gaussian illumination profile used in the present apparatus was unnecessarily narrowed relative to the instrumental full aperture. This is, in fact, not the case. One crucial detail which has been omitted in obtaining the results presented in Figs. 7 and 8 is the possible vignetting effect of the instrument's maximum aperture. In calculating $E_0(\xi)$ for the gaussian $E_0(x)$, for example, the integral in eq. (40) was taken over all x, thereby neglecting any aperturing effects that might occur.

For the actual VSA scattering instrument, which has a fixed maximum aperture, b, $E_0(\xi)$, and $E_0(x)$ are related via the finite domain transform

$$E_0(\xi) = \frac{1}{(f\lambda_0)^{\frac{1}{2}}} \int_{-b/2}^{b/2} E_0(x) e^{i(2\pi/f\lambda_0)\xi x} dx. \tag{46}$$

Except for a few special cases, an analytical evaluation of this integral is not possible, and one must resort to a numerical approach to investigate various apodizing schemes. For the experimentally relevant case of gaussian illumination, eq. (46) becomes

$$E_0(\xi) = \frac{E_0}{(f\lambda_0)^{\frac{1}{2}}} \int_{-b/2}^{b/2} e^{-x^2/2\sigma^2 + i(2\pi/f\lambda_0)\xi x} dx. \tag{47}$$

On completing the square in the exponential and a change of variable, we can rewrite this expression in the form

$$E_0(\xi) = \frac{E_0}{(f\lambda_0)^{\frac{1}{2}}} \sqrt{2\sigma} e^{-(\sigma^2 K^2/2)} \int_{w_-}^{w_+} e^{-w^2} dw, \tag{48}$$

where K, w, w_+, and w_- are defined as follows:

$$\begin{aligned} w &= \frac{x}{\sqrt{2}\sigma} - i\frac{\sigma K}{\sqrt{2}} \\ K &= (2\pi/\lambda_0)\frac{\xi}{f} \\ w_+ &= +\frac{b}{2\sqrt{2}\sigma} - i\frac{\sigma K}{\sqrt{2}} \\ w_- &= -\frac{b}{2\sqrt{2}\sigma} - i\frac{\sigma K}{\sqrt{2}}. \end{aligned} \tag{49}$$

The analyticity of $\exp(-w^2)$ near $w = 0$ allows the complex plane w integral to be split into two terms, each having the form of an error function of complex argument. Tabulated values of this function are available in the literature[36] for a restricted range of the parameters (b/σ) and (σK).

In searching out an optimum configuration for the MK VI instrument, it was decidely more convenient to adopt a fully numerical approach in evaluating eq. (47). Appendix B outlines the methods that were used. The modified instrumental profile calculations were carried out for a range of values of the ratio (b/σ) with the aperture opening, b, held fixed at $b = b^* = 5.0$ cm.

Figure 9 shows four such profiles plotted in terms of the normalized intensity ratio $I_0(\theta)/I_0(0)$. Also shown are the corresponding aperture ratios $I_0(x)/I_0(0)$. The curve for $(b/\sigma) = 0.01$ is essentially equivalent to the result obtained above for uniform aperture illumination. The most striking feature of the remaining three $I_0(\theta)/I_0(0)$ curves is the presence of an effective background or floor contribution to the profile caused by edge diffraction at the aperture. This "shelf" or wing on the profile has the slow oscillatory decay of a $(\sin^2 x)/x^2$ functional dependence. In each case, however, the $\theta \approx 0$ portion of the curves closely approximates the gaussian profile expected from unapertured gaussian illumination.

The results given in Fig. 9 clearly illustrate the tradeoff involved in selecting a value of σ. In circumstances requiring an instrumental line shape with a very low background level, we are forced to accept a moderate increase in $\delta\theta(\frac{1}{2})$ and, therefore, a loss in angular resolving power. The curve given in Fig. 9 for $(b/\sigma) = 6.05$ corresponds to the choice that was made for the MK VI apparatus. Various half-width values for this profile have been included in Table IV for comparison with the results for unapertured gaussian and uniform illumination. In the actual instrument, this choice for (b/σ) guarantees that the calculated edge-diffraction "floor" constitutes less than 10 percent of the overall stray-light level. This point is illustrated in Fig. 10 which

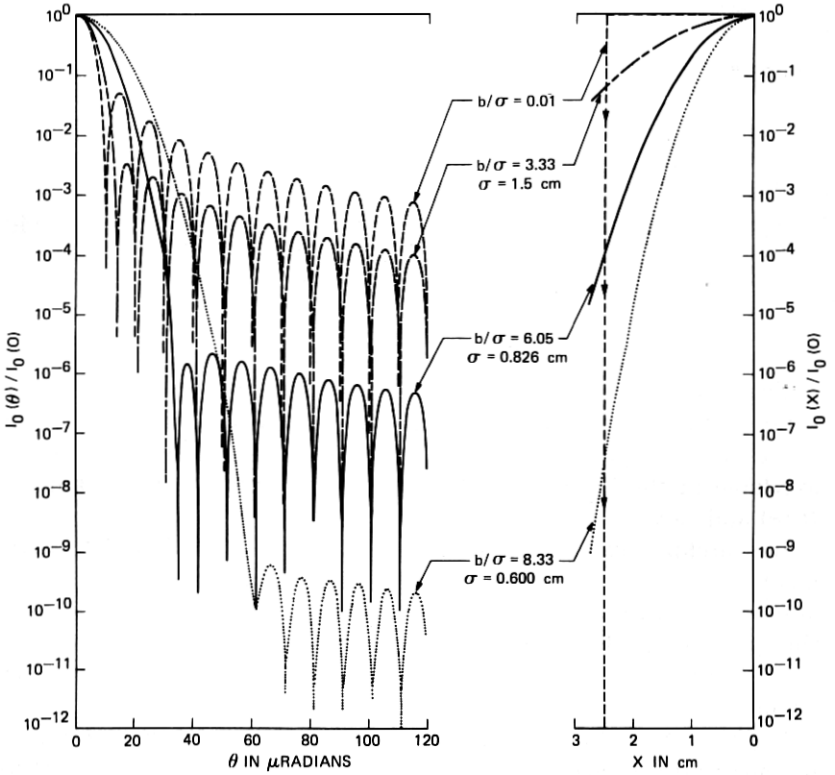

Fig. 9—Calculated instrumental profiles for truncated gaussian illumination and various values of (b/σ). Also shown, on a logarithmic intensity scale, are the corresponding normalized illumination functions $[I_0(x)/I_0(0)]$. The curves labelled $(b/\sigma) = 6.05$ are appropriate to the b and σ values used in the present apparatus.

shows the theoretical profile for $(b/\sigma) = 6.05$ superimposed on the measured profiles of the MK IV instrument.

At this point, it is crucial to realize that the truncated transform results apply not only downstream from the aperture plane of Fig. 6 but also upstream toward the spatial filter. There are, in fact, two other possible sources of beam vignetting in the system. The most obvious is the spatial filter itself. Since the field at the spatial filter and the field at the aperture plane are Fourier transform pairs, the same considerations involved in choosing (b/σ) also apply to the choice of spatial filter pinhole size. If edge-diffraction effects at the aperture plane are to dominate the system profile, then the ratio of pinhole diameter, b_{PH}, to the gaussian focal width at the pinhole, $d_{\xi'}(1/e)$, must exceed (b/σ). Specifically, for the present instrument, b_{PH} must satisfy the inequality

$$\frac{b_{PH}}{9.6\,\mu\text{m}} > \frac{b}{\sigma} = 6.05$$
$$b_{PH} > 58\,\mu\text{m}. \tag{50}$$

The pinhole diameter actually used is $b_{PH} = 100\ \mu m$. We note that a $[b_{PH}/d_{\xi'}(1/e)]$ ratio this large is contrary to usual spatial filtering practices.

A much more subtle source of possible beam aperturing is the internal cavity configuration of the laser source itself. Clearly, the ratio of laser tube inside diameter, b_{LASER}, to the mode $(1/e)$ radius, σ_{LASER}, must also satisfy the inequality

$$\frac{b_{\text{LASER}}}{\sigma_{\text{LASER}}} > \frac{b}{\sigma}. \tag{51}$$

The laser used in the MK VI has a gaussian mode diameter given as

$$D_{\text{LASER}}(1/e^2) = 1.4\ \text{mm}, \tag{52}$$

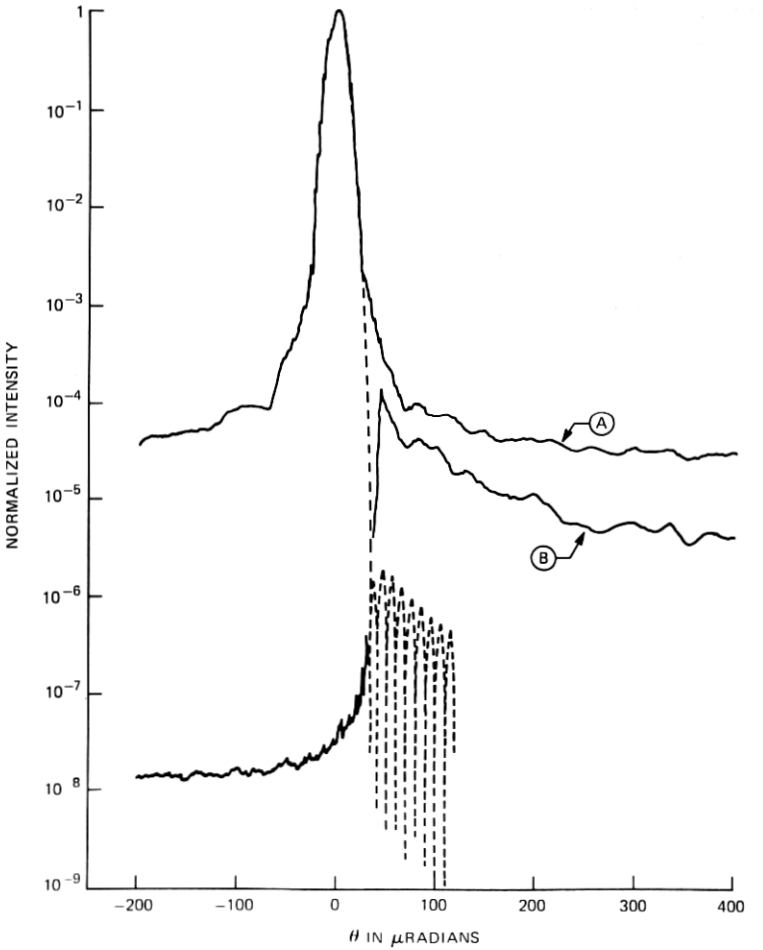

Fig. 10—Calculated instrumental profile for truncated gaussian illumination (dashed curve) superimposed on the measured profiles of the MK VI instrument. Curves A and B correspond to the two measurements described in Fig. 4.

which is equivalent to

$$\sigma_{\text{LASER}} = \frac{D_{\text{LASER}}(1/e^2)}{2\sqrt{2}} \cong 0.5 \text{ mm}. \tag{53}$$

The plasma tube ID for the laser is $b_{\text{LASER}} = 5.0$ mm yielding a b/σ ratio

$$\frac{b_{\text{LASER}}}{\sigma_{\text{LASER}}} \cong 10. \tag{54}$$

Therefore, in the MK VI instrument, the maximum design aperture available to the collimated beam is, in fact, the principal source of truncation effects.

In situations where it is advantageous to alter this resolution-background tradeoff by varying (b/σ), it soon becomes apparent that the numerical profile calculations of Appendix B are a rather unwieldy design tool. Instead, based on an examination of the results shown in Fig. 9, it seemed tempting to fit the profile tails to the form

$$\frac{I_T(\theta)}{I(0)} = A_1 \frac{\sin^2 (k_0 b\theta/2)}{(k_0 b\theta/2)^2} \tag{55}$$

and look for an interpolation formula relating the amplitude A_1 to the ratio (b/σ). By a trial-and-error procedure, the following relation was found to reproduce the best-fit A_1 values to within 10-percent error:

$$A_1^* = \left(1 + \frac{b^2}{8\sigma^2}\right) e^{-b^2/4\sigma^2}. \tag{56}$$

Table V gives the fitted and interpolated values of A_1 corresponding to the four (b/σ) ratios of Fig. 9. It is interesting to note that the exponential factor $\exp(-b^2/4\sigma^2)$, which dominates the (b/σ) dependence, is just the normalized aperture illumination at the aperture edge.

3.2 Optical aberrations

The fundamental diffraction limitations set out in Section 3.1 are really only a prediction regarding the ideal performance of an optical system. In the final analysis, the inherent optical aberrations of any particular apparatus design determine how close one will come to achieving the ideal of diffraction-limited performance. In this section, we give a brief summary of those aspects of optical aberration theory[37] that are relevant to the design of the MK VI apparatus. From a qualitative understanding of and analytical expressions for each of the various aberrations, we then determine the extent to which aberrations modify the ideal diffraction-limited characteristics of the instrument.

Table V — Fractional amplitude of the edge diffraction contribution to the instrumental profile of truncated gaussian illumination. The first column gives the A_1 values obtained by fitting eq. (55) to the tails of the profiles shown in Fig. 9; the second column gives the A_1 value predicted by the interpolation formula in eq. (56)

(b/σ)	A_1-Fitted	A_1^*-Interpolated
0	1.0	1.0
3.333	1.33×10^{-1}	1.49×10^{-1}
6.05	5.823×10^{-4}	5.92×10^{-4}
8.333	2.782×10^{-7}	2.79×10^{-7}

Finally, a number of measurements taken on the MK VI instrument are compared to the quantitative predictions of the aberration theory.

Because the present instrument is illuminated with monochromatic light, the various chromatic aberrations are absent, and the lowest-order non-zero distortions come from the third-order or primary aberrations. Here we follow the order-naming convention associated with the Taylor expansion of the function $\sin \psi$, i.e.,

$$\sin \psi = \psi - \frac{\psi^3}{3!} + \frac{\psi^5}{5!}, \tag{57}$$

where ψ is the angle of incidence of a ray on a reflecting or refracting surface. The approximation $\sin \psi = \psi$ leads to the usual paraxial optics formulae. The next term in the expansion, proportional to ψ^3, describes the primary aberrations.

The principle aberration-producing elements of the MK VI apparatus are the off-axis spherical mirrors M_5 and M_6 (see Fig. 1). Figure 11 shows the basic optical configuration in which the mirrors are used. The labelled geometrical parameters are:

$$\begin{aligned} u_p = \frac{\gamma}{2} &\text{—The half-field angle or off-axis angle} \\ \mathcal{a} &\text{—The semi-aperture} \\ R &\text{—The mirror radius of curvature.} \end{aligned} \tag{58}$$

The primary aberrations for an off-axis spherical mirror depend parametrically on two angles: u_p, the half-field angle and $(\mathcal{a}/R)$, the semi-aperture angle. The aberrations associated with the various

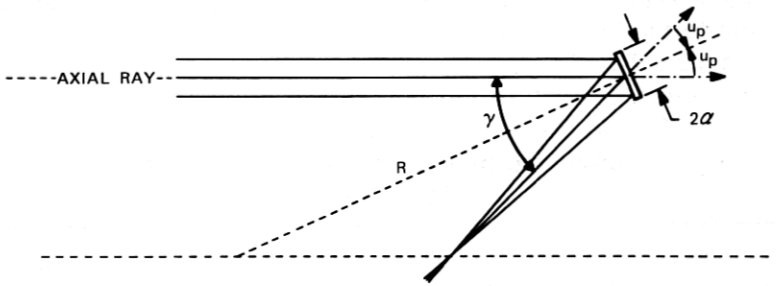

Fig. 11—Off-axis mirror configuration used in the MK VI instrument showing the important geometrical parameters.

third-order products of these angles are:

$$\begin{aligned} (\alpha/R)^3&\text{—Spherical aberration}\\ (\alpha/R)^2 u_p&\text{—Coma}\\ (\alpha/R) u_p^2&\text{—Astigmatism}\\ u_p^3&\text{—Distortion.} \end{aligned} \tag{59}$$

3.2.1 Spherical aberration

Spherical aberration is a longitudinal focussing defect that is present even when the off-axis angle goes to zero. Figure 12 sketches the basic ray geometry for a spherical mirror exhibiting pure spherical aberration. As illustrated in the enlarged detail of the sketch, the marginal rays of an incoming parallel bundle are brought to a focus at a point closer to the mirror's surface than those lying nearer the axial ray. This constantly changing longitudinal focal position results in a transversely smeared focal spot rather than a focal point.

One common measure of the amount of spherical aberration is the minimum beam waist size produced in the focal region. For a spherical reflector, the diameter of this blur spot is given by

$$2TSC^* = \alpha^3/R^2. \tag{60}$$

Since transverse displacement at the focus is equivalent to an angular deviation in the parallel bundle, we can also express the spherical aberration in terms of a full-width angular blur,

$$\Delta\theta^*_{SC} = \frac{2TSC^*}{f} = 2(\alpha/R)^3, \tag{61}$$

where $f = R/2$ is the focal length of the reflector.

3.2.2 Astigmatism

Astigmatism, like spherical aberration, is the result of a longitudinal focussing defect. In contrast to the spherical aberration defect, how-

ever, the longitudinal focussing error depends not on aperture diameter, $2\mathcal{Q}$, but on the off-axis angle, u_p. Figure 13 illustrates the ray geometry of pure astigmatism for a spherical reflector.

One of the fundamental characteristics of the u_p dependent aberrations is the loss of rotational symmetry in the focal region. A non-zero off-axis angle destroys this symmetry and establishes two unique directions or planes of transverse blurring. The plane defined by the incident and reflected axial ray is the tangential plane. Cartesian or angular displacements perpendicular to the axial ray and lying in this plane are referred to as tangential displacements. The two planes orthogonal to this tangential surface and containing either the incident or reflected axial ray are called the sagittal planes. Cartesian or angular displacements from the axial ray in these planes are sagittal displacements.

For a spherical reflector exhibiting pure astigmatism, a fan of parallel tangential plane rays are brought to a focus closer to the mirror surface than an identical sagittal fan. The focal region pattern found by decomposing the entire illuminated aperture into such ray fans consists of the two longitudinally separated focal lines depicted in Fig. 13a. The longitudinal ($\hat{z}$) separation of the S and T foci ($2AC^*$)

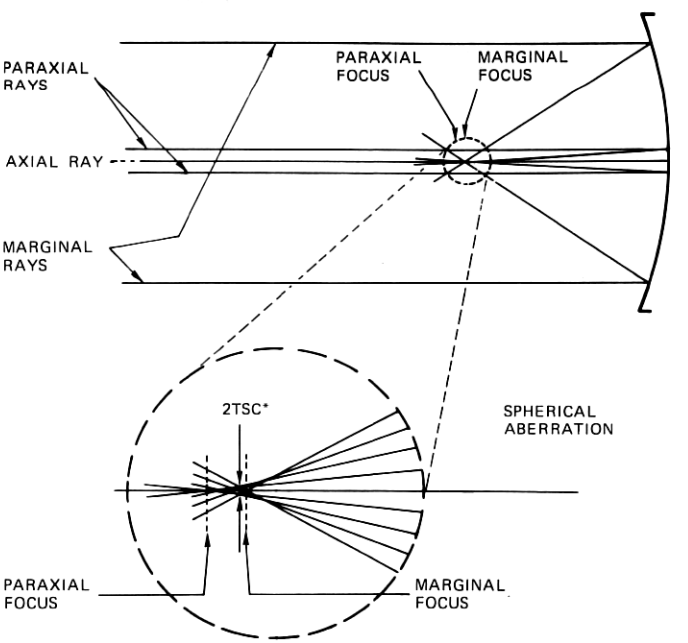

FIG. 12—Ray diagram for a single spherical mirror exhibiting a pure spherical aberration defect.

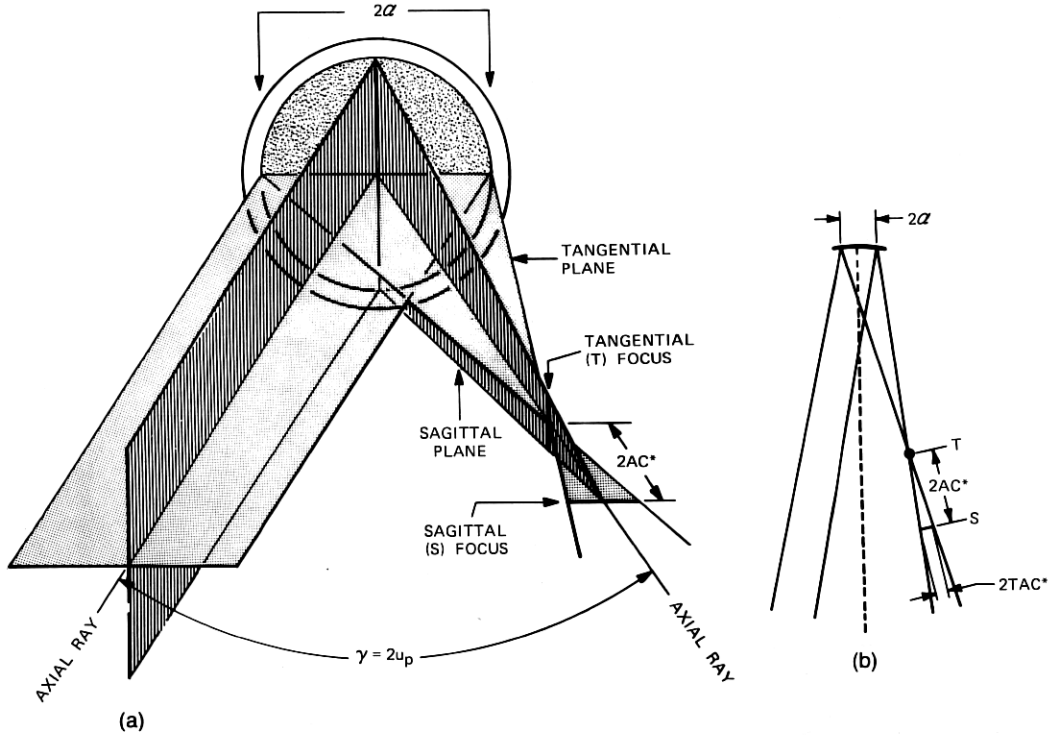

Fig. 13—Partial ray diagram illustrating the focal plane characteristics of an off-axis spherical mirror exhibiting the pure astigmatism defect.

can be calculated from the relation

$$AC^* = \frac{Ru_p^2}{4} \tag{62}$$

and depends only on the semi-field angle.

In the absence of other aberrations (and the effects of diffraction), the S and T focal lines are infinitely narrow in their respective planes. This means that the sagittal height of the tangential focus and the tangential width of the sagittal focus can be obtained from simple extremal ray geometry. For example, Fig. 13b shows the extremal rays seen in a tangential plane projection. Normally $2AC^*$ is small compared to the reflectors focal length $(R/2)$. It follows that the lengths of the two focal lines are identical and given by

$$2TAC^* = 2AC^*\left(\frac{2\mathcal{A}}{R/2}\right) = 2\mathcal{A}u_p^2. \tag{63}$$

The full-width angular spread equivalent to this spatial blur is

$$\Delta\theta_{TAC^*} = 4(\mathcal{A}/R)u_p^2. \tag{64}$$

3.2.3 Coma

When the off-axis angle is non-zero, the longitudinal focussing error that produces spherical aberration also gives rise to an asymmetric transverse blurring called coma. Figure 14a sketches the basic elements of the focal region pattern for a spherical reflector exhibiting a pure coma defect. Rays in the paraxial region are brought to a focus at the axial focus, P, while rays from larger-diameter annular zones on the mirror's surface form focal circles whose centers are tangentially displaced from P. The radius of a particular focal circle increases as the square of the radius of the zone producing it.

Figure 14b gives a qualitative representation of the characteristics of the focal pattern as found by dividing up the illuminated aperture into these annular zones. Mathematically speaking, the focal circles are not sharp unless the radial thickness of the corresponding zones vanish; however, the sketch does predict quite nicely the overall exterior outline of the coma blur patch.

The continuum of focal circles nest into a 60° wedge extending out from the axial focus forming a pattern commonly called comatic flare. The largest-diameter focal circle, produced by the annular zone at the edge of the illuminated aperture, has a radius CC^* given by

$$CC^* = \frac{\mathcal{A}^2 u_p}{2R}. \tag{65}$$

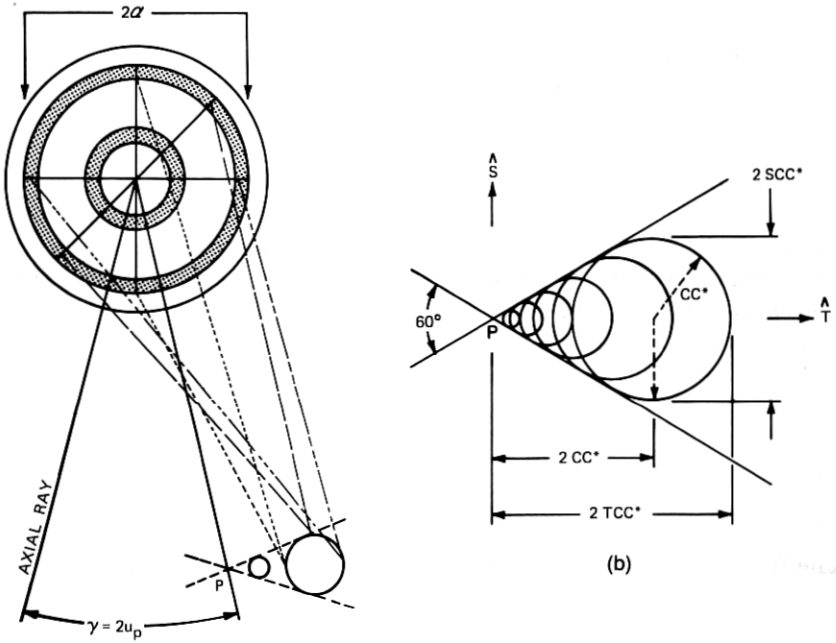

Fig. 14—Partial ray diagram, (A), of an off-axis spherical mirror exhibiting a pure coma defect. The details of the focal plane pattern are illustrated in (B).

Its center is tangentially displaced from the axial focus by an amount $2CC^*$.

Although coma is a highly asymmetric aberration, it is still convenient to specify its effect in terms of transverse and/or angular blur sizes. The numbers ordinarily quoted for coma correspond to the extremal dimensions of the coma patch in the tangential and sagittal directions. It follows easily from Fig. 14b that the full-width transverse spatial blurs are

$$\begin{aligned} \hat{T} \text{ DIRECTION} \quad & 2TCC^* = 3CC^* = \frac{3\mathcal{A}^2 u_p}{2R} \\ \hat{S} \text{ DIRECTION} \quad & 2SCC^* = 2CC^* = \frac{\mathcal{A}^2 u_p}{R}. \end{aligned} \tag{66}$$

The equivalent full-width blur angles are

$$\begin{aligned} \hat{T} \text{ DIRECTION} \quad & \Delta\theta^*_{TCC} = 3(\mathcal{A}/R)^2 u_p \\ \hat{S} \text{ DIRECTION} \quad & \Delta\theta^*_{SCC} = 2(\mathcal{A}/R)^2 u_p. \end{aligned} \tag{67}$$

3.2.4 Distortion

The last of the primary aberrations is a defect of off-axis magnification called distortion. This particular aberration is associated principally with optical systems that form a real image of an extended object at finite magnification. For example, the image of a rectangular grid of regularly spaced points will exhibit the classic "barrel" or "pincushion" appearance in an optical system involving pure distortion. For the situation of interest here, namely a spherical reflector with the image at infinity or at the focus, the amplitude of the pure distortion aberration vanishes identically.

3.2.5 Application of the aberration results to the MK IV instrument

The third-order aberration theory results for the off-axis spherical reflector are summarized in Table VI which gives the expressions for the various transverse and angular blurs. It must be emphasized that the aberration theory results outlined above are derived from purely geometric ray tracing. In no sense does this theory predict the actual intensity distribution in the image plane for a specific aperture illumination. The transverse and angular blur patterns define the outlines of a boundary between focal illumination and strict geometric shadow in the absence of all wave interference and diffraction effects. However, in certain situations, it is possible to combine the geometric aberration results with aberration-free diffraction calculations to obtain useful instrumental profile information. The approach works well when one or more of the following conditions are satisfied:

(*i*) Diffraction blurring is large or small compared to spherical aberration.

(*ii*) One primary aberration is dominant.

(*iii*) The ideal diffraction-limited system profile is free of large interference maxima and minima.

Table VI — Summary of the analytic expressions for the transverse and angular aberration blurs for a single off-axis spherical mirror

Aberration	Full-Width Transverse Blur	Full-Width Angular Blur
Spherical	$\mathfrak{a}^3/R^2 \quad (2\,TSC^*)$	$2(\mathfrak{a}/R)^3$
Coma	$\hat{T} \quad -3\mathfrak{a}^2 u_p/2R \quad (3\,CC^*)$ $\hat{S} \quad -2\mathfrak{a}^2 u_p/2R \quad (2\,CC^*)$	$-3(\mathfrak{a}/R)^2 u_p$ $-2(\mathfrak{a}/R)^2 u_p$
Astigmatism	$2\mathfrak{a}u_p^2 \quad (2\,TAC^*)$	$4(\mathfrak{a}/R)u_p^2$
Distortion	$Bu_p^3 R$	$2\,Bu_p^3$

In these cases, one can intuitively construct the aberration-affected profiles with a fair degree of accuracy using the one-to-one geometric mapping of regions of the aperture onto the focal plane. For example, it can be argued from Fig. 13b that for pure astigmatism the tangential direction intensity profile at the sagittal focus should be a demagnified replica of the aperture illumination. This type of analysis is essential in obtaining quantitative results from the aberration expressions.

In the MK VI instrument, the off-axis angle and radii of mirrors M_5 and M_6 are

$$\begin{aligned} \gamma &= 2|u_p| = 0.116 \text{ rad} \\ R &= 200 \text{ cm}. \end{aligned} \tag{68}$$

Assigning a value to be used for the semi-aperture $\mathfrak{A}$ is a more subtle question, especially since we are interested in gaussian rather than uniform aperture illumination. However, in the spirit of the astigmatism example given in the preceding paragraph, we take

$$\mathfrak{A} = d_x(1/e) = \sigma^* = 0.826 \text{ cm} \tag{69}$$

and *assume* that the focal plane profiles will also be gaussian. On the basis of geometrical imaging, the blur values calculated via Table VI should then be (with the exception of coma) the full-width to the $(1/e)$ points of a focal plane gaussian profile. We show in succeeding paragraphs that these assumptions lead to a selfconsistent picture of the experimentally observed aberration effects in the MK VI instrument.

Table VII gives the transverse and angular blurs for a single spherical reflector in the MK VI configuration. The table also includes the longitudinal separation of the S and T focal planes as well as the full angular width of the focus imposed by diffraction. From the viewpoint of small-angle-scattering performance, the most serious of the aber-

Table VII — Numerical values of the aberration blurs for a single spherical mirror used in the MK VI configuration

Aberration	Full-Width Transverse Blur (μm)	Full-Width Angular Blur (μrad)
Spherical	0.141	0.141
Coma	$\hat{T}$ 2.96	2.96
	$\hat{S}$ 1.97	1.97
Astigmatism	55.6	55.6
Distortion	0	0

$(S\text{-}T)_{\text{separation}} = 2\,AC^* = 0.336$ cm. $\Delta\theta(1/e)_{\text{diffraction}} = 19.3$ μrad.

Table VIII — Numerical values of the aberration blurs for the system of two off-axis spherical mirrors used in the MK VI apparatus

Aberration	Full-Width Transverse Blur (μm)	Full-Width Angular Blur (μrad)
Spherical	0.282	0.282
Coma	T 0 S 0	0 0
Astigmatism	111.2	111.2
Distortion	0	0

$(S\text{-}T)_{\text{separation}} = 2(2\,AC^*) = 0.672$ cm. $\Delta\theta(1/e)_{\text{diffraction}} = 19.3$ μrad.

rations is coma. Even though the calculated comatic blurs are numerically small compared to the diffraction spread, the presence of coma can result in a distinctly asymmetric instrumental profile. Moreover, in a coherently illuminated system, the coma flare is criss-crossed by interference patterns whose tails extend far beyond the calculated geometric limits. This latter effect can significantly raise the effective "floor" level of the instrumental profile.

Fortunately, in a symmetric two-mirror system like the MK VI, the geometry may be chosen such that the total coma vanishes identically. In fact, all aberrations that depend on an odd power of the half-field angle u_p disappear if the field angles at the two elements are made equal and of opposite sign. By convention, u_p is defined as the angle through which the incoming axial ray must be rotated to bring it into coincidence with the local radius vector of the element's spherical surface (see Fig. 8). An inspection of Fig. 1 shows that in the MK VI apparatus the field angle rotations at M_5 and M_6 are of opposite sense. In this case, when the two off-axis angles are made equal in magnitude the coma and distortion aberrations vanish while the spherical aberration and astigmatism double.

The total calculated aberration blurs for the instrument are summarized in Table VIII. Since the spherical aberration is small compared to the diffraction spread, it is reasonable to expect that the interpretation of these blur values as $(1/e)$ full-widths of a gaussian blur profile should work quite well. This is in fact the case.

The tangential and sagittal foci of the MK VI instrument were located using a modified Foucault knife-edge procedure, and $\hat{T}$ direction scans of the intensity profiles were taken in each case. The measured S-T separation was

$$(S\text{-}T) \text{ separation} = 0.660 \pm 0.013 \text{ cm.} \tag{70}$$

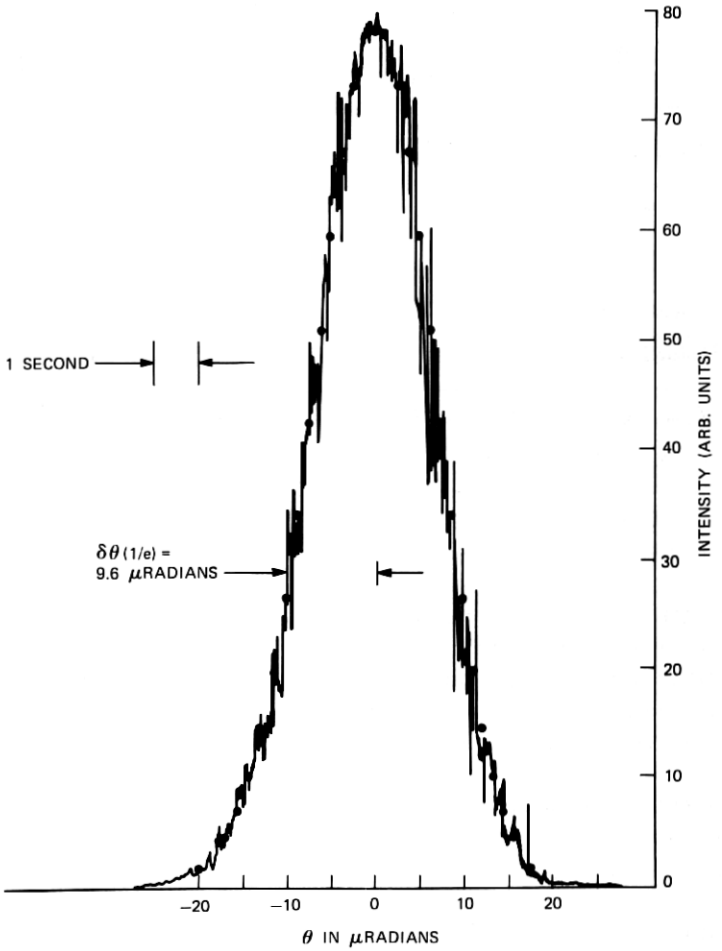

Fig. 15—Observed instrumental profile as measured by a tangential direction scan in the instrument's tangential focal plane. The heavy dots are a best fit to the function $\exp[-\theta^2/\delta\theta^2(1/e)]$.

At the T focus, only diffraction and spherical aberration contribute to the profile width. From the standard gaussian convolution formula, we can calculate the expected $\Delta\theta(1/e)$:

$$\begin{matrix} T \text{ PLANE} \\ \hat{T} \text{ SCAN} \end{matrix} \quad \Delta\theta(1/e) = \sqrt{(19.30)^2 + (0.282)^2}\ \mu\text{rad} = 19.302\ \mu\text{rad}. \tag{71}$$

Clearly the spherical aberration has a negligible effect on the ideal diffraction-limited broadening. Figure 15 shows a typical high-resolution T-plane scan for the instrument. The large apparent noise in this

trace is produced by residual air currents and vibration in the apparatus and corresponds to a peak-to-peak beam wander of roughly 0.5 μrad (0.7 arc second). The results of fitting the observed profile with a gaussian shape are indicated by the points in Fig. 15 and give an experimental full width

$$\Delta\theta(1/e) = 2\delta\theta(1/e) = 19.2\ \mu\text{rad}. \tag{72}$$

In the S focal plane, diffraction, astigmatism, and spherical aberration all contribute to the instrumental line shape. The full-width calculated from Table VIII is

$$\begin{matrix} S \text{ PLANE} \\ \hat{T} \text{ SCAN} \end{matrix} \quad \Delta\theta(1/e) = \sqrt{(19.3)^2 + (0.282)^2 + (111.2)^2}\ \mu\text{rad}$$
$$= 113\ \mu\text{rad}. \tag{73}$$

The predicted width comes predominately from the astigmatic blurring. Figures 16 and 17 give two experimental S-plane profiles recorded with logarithmic and linear intensity scales, respectively. A gaussian

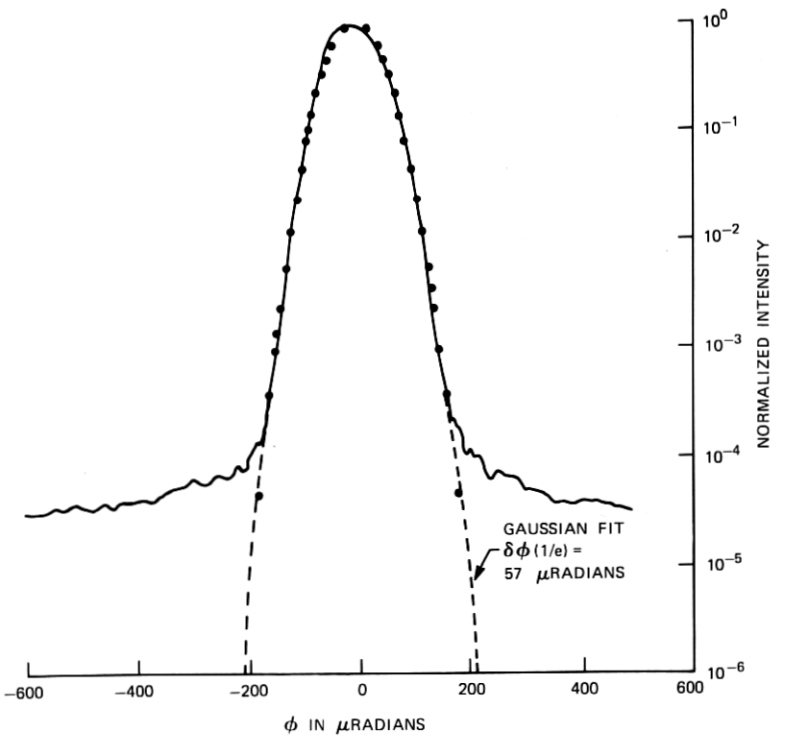

Fig. 16—Observed instrumental profile as measured by a tangential direction scan in the instrument's sagittal focal plane. The heavy dots and dashed curve a are best fit to the function exp $[-\varphi^2/\delta\varphi^2(1/e)]$.

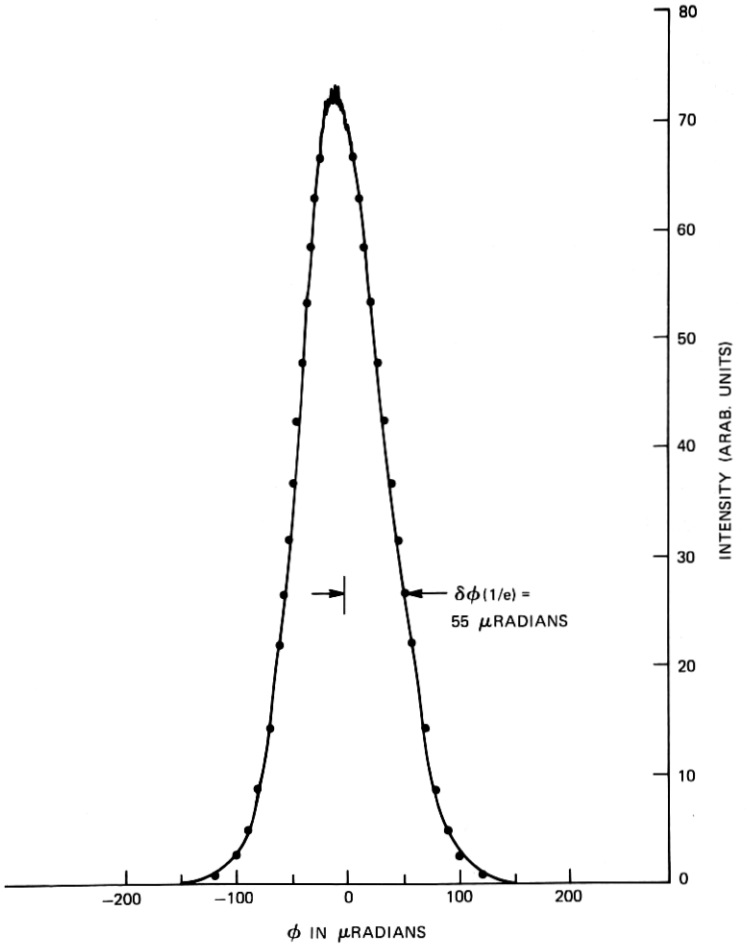

Fig. 17—Observed instrumental profile as measured by a tangential direction scan in the instrument's sagittal focal plane. The heavy dots are a best fit to the function $\exp[-\varphi^2/\delta\varphi^2(1/e)]$.

fit to the logarithmic curve, indicated by the points in Fig. 16, gives very good agreement with the observed line shape over roughly four orders of magnitude in intensity. The range and precision of the fit provide strong support to our assumptions regarding the interpretation of the aberration blur values. The best-fit half-width values for the logarithmic and linear scans are $\delta\theta(1/e) = 57$ μrad and $\delta\theta(1/e) = 55$ μrad, respectively. The mean observed full-width

$$\Delta\theta(1/e) = 112\ \mu\text{rad}$$

is in excellent agreement with the calculated value given in eq. (73).

3.2.6 Conclusions

In summarizing the discussion of aberrations, a number of general points deserve to be made and reiterated regarding the relationship between aberrations and small-angle-scattering performance.

(*i*) The cancellation of the asymmetric aberrations, coma especially, is crucial in obtaining an instrumental profile that has symmetry, the necessary steep skirt fall-off, and a low background value.

(*ii*) Spherical aberration, although it has a negligible effect relative to diffraction in the present instrument, can rapidly grow to serious proportions with increasing aperture size, $\mathfrak{a} = d_x(1/e)$. The angular blur of this aberration, $\Delta\theta^*_{SC}$, increases as the cube of the aperture size while the diffraction spread varies inversely with $d_x(1/e)$. The relative contribution of spherical aberration to the profile width will, therefore, increase as $\mathfrak{a}^4$. Since $\Delta\theta^*_{SC}$ depends only on the reduced quantity $(\mathfrak{a}/R)$, however, a constant ratio of spherical blur to diffraction spread can always be obtained by scaling the mirror radius R to keep $\mathfrak{a}^4/R^3$ constant. For example, an instrument with 10 times better angular resolution than the MK VI might conceivably utilize 80-cm-diameter mirrors with a 21.5-meter focal length.

(*iii*) The presence of a large residual astigmatism need not be detrimental if one is satisfied with an instrumental performance that is diffraction limited in only a single angular direction. It might appear from Fig. 13 that simultaneous sagittal and tangential resolution could be achieved by placing separate slits at the S and T foci of the collecting mirror. This is true if the wavefronts of the incoming ray bundle are perfectly parallel. However, in a two-mirror symmetric apparatus, such a bundle cannot be produced because of the collimating mirror astigmatism. For example, with reference to Fig. 1, the spatial filter pinhole, A_2, can be placed at either the T or S focus of mirror M_5. In the first case, the wavefronts of the beam travelling toward M_7 are tangentially collimated but sagittally curved; in the second case, the converse is true. From the viewpoint of light-scattering kinematics, this "collimated" beam will be able to conserve momentum with a relatively broad range of scattering vectors lying in the plane containing the wavefront curvature. Thus, even though mirror M_6 forms S and T focal lines of equal sharpness, only a single high-resolution axis actually exists for either position of pinhole A_2.

In the MK VI instrument, the spatial filter pinhole is at the T focus of the collimating mirror so that the probe beam is tangentially collimated. The nature of the wavefront curvature in the sagittal plane may be calculated in a simple fashion from the known (S-T) separation $2AC^*$. Since the pinhole (at the T focus) is closer to the mirror's surface

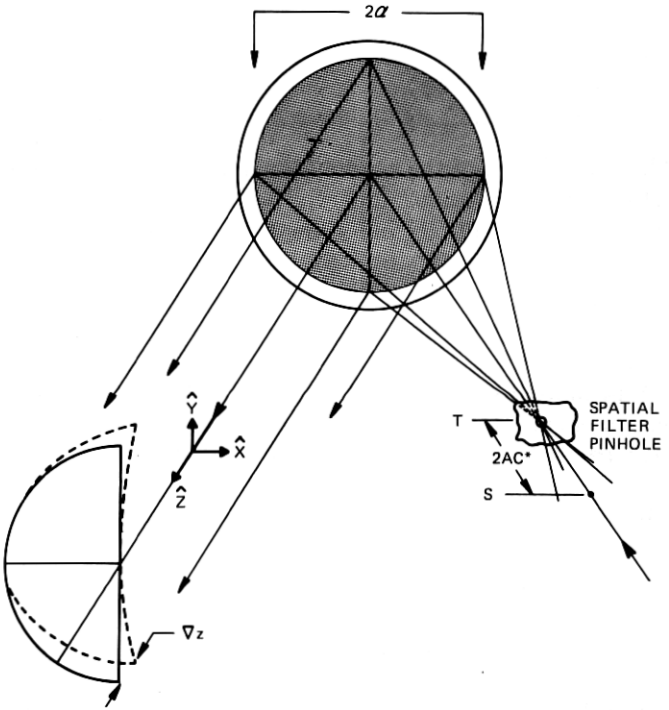

Fig. 18—Illustration of the wavefront curvature existing in the off-axis mirror collimating arm of the MK VI instrument.

than the S focus, the sagittal plane wavefronts appear to diverge from a point source lying behind the mirror. The object distance, q, between this virtual point source and the mirror, may be calculated via the usual paraxial formula. Since $(S\text{-}T) = 2AC^*$ is small compared to the focal length of M_5, we have

$$q \cong \frac{f^2}{2AC^*} = \frac{R^2}{4(2AC^*)}. \tag{74}$$

Inserting the appropriate numerical values, $R = 200$ cm and $2AC^* = 0.336$ cm, gives

$$q \cong 3.98 \times 10^4 \text{ cm}. \tag{75}$$

Figure 18 shows a sketch of the probe-beam constant-phase surfaces with the sagittal curvature greatly exaggerated for clarity. The magnitude of the curvature can be specified in terms of the longitudinal spatial separation between the wavefront and a reference plane which is tangent to the wavefront at the axial ray. Since the virtual sagittal source point lies so far behind the mirror, it does not matter exactly

where in the optical path we calculate this separation. The maximum deviation between the wavefront surface and the reference plane, ∇z, occurs at the sagittal extremes of the beam and is easily found to be given by

$$\nabla z = \frac{\mathcal{A}^2}{2q}. \tag{76}$$

If we take $\mathcal{A} = b^*/2$, where $b^* = 5.0$ cm is the maximum clear aperture diameter in the MK VI instrument, we have

$$\nabla z \cong 10.5 \times 10^{-5} \text{ cm},$$

or roughly 2λ of peak deviation from perfect collimation. In a situation where the full sagittal ($\hat{y}$) aperture height need not be used, it is possible to reduce this deviation substantially since ∇z is proportional to $\mathcal{A}^2$. For example, if we aperture the height of the probe beam to $b = 5$ mm, the peak wave-front deviation is reduced to $\nabla z \cong \lambda/50$, or essentially perfect collimation. Thus, the most desirable probe-beam configuration in the MK VI instrument corresponds to a "flat ribbon" or "sheet" type of illumination.

3.3 Scattered field intensity, spatial coherence, and scattering kinematics in the presence of aberrations

In a light-scattering optical system whose angular resolution capabilities are in some respect dominated by aberration effects—for example, the astigmatic φ blurring in the present instance—we find that other important properties of the observed scattered field are modified by the aberrations as well. In this section, we examine three aspects of normal light-scattering theory that are qualitatively altered by the presence of aberrations:

(*i*) The form of the spatial coherence function for the scattered field.

(*ii*) The application of the normal kinematic restrictions (or wave vector conservation conditions) in the scattering process.

(*iii*) The calculation of the amplitude of the perturbations that give rise to observed levels of scattered or stray light.

The effects of aberrations in all three cases have a straightforward physical interpretation connected with the fact that light scattered into a specific direction (θ, φ) is no longer brought to a diffraction-limited spot focus at the observation plane.

In typical calculations of the scattered field, in which an incoming plane wave is assumed to impinge on the sample, the far-field angular distribution of scattered intensity is shown to be simply the spatial Fourier transform of the refractive-index perturbations in the illumi-

nated volume.[1,3] The light observed at a particular angular position (θ, φ) is contributed by a Fourier component of the refractive index $\mathbf{K}$ given by

$$\mathbf{K} = \mathbf{k}_s - \mathbf{k}_0, \tag{77}$$

where $\mathbf{k}_0$ is the wave vector of the incident beam and $\mathbf{k}_s$ points in the direction of observation (θ, φ) and has a magnitude $|\mathbf{k}_s| = |\mathbf{k}_0| = 2\pi/\lambda_0$. For a finite illuminated volume, the refractive-index perturbations are most usefully represented in terms of a plane-wave Fourier expansion

$$\sum_j \delta n_j \exp(i\mathbf{K}_j \cdot \mathbf{r}'), \tag{78}$$

with the $\mathbf{K}_j$ chosen to make the expansion functions orthonormal over the scattering volume.[27] The scattering of a collimated incident beam by this assembly of plane waves consists of a family of diffracted beams that originate from the $\mathbf{K}_j$'s satisfying the Bragg condition, eq. (77). On the surface of a sphere in the far field, these diffracted beams form a contiguous but essentially nonoverlapping series of diffraction "spots," each associated with a particular $\mathbf{K}_j$. In the usual situation, where the amplitudes of the individual $\mathbf{K}_j$ disturbances are statistically independent, these patterns also delineate areas or solid angles of statistical field correlation. If the far-field scattered radiation is focussed onto the observation plane by an ideal lens or mirror, this contiguous angular distribution of "spots" is imaged one-for-one onto the focal plane. A ray penetrating the reference sphere at an angular position (θ, φ) is imaged onto the focal plane at a transverse position (ξ, η), where, in the small angle limit,

$$\xi = f\theta, \qquad \eta = f\varphi. \tag{79}$$

In this ideal situation, the intensity observed at some (ξ, η) is scattered essentially by a single $\mathbf{K}_j$ plane-wave mode. The measured intensity may, in theory, be used to calculate the mean-square-amplitude of the mode, or vice-versa. Furthermore, the spatial coherence properties of the field at the observation plane are determined uniquely by the angular distribution of intensity within *one* of the diffracted beams.

Formally speaking, the presence of aberrations in the imaging of the reference sphere scattered field produces qualitatively the same effects as any other imperfect focussing of the far-field pattern. The pattern of diffraction spots will be formed with a degree of spot broadening and overlap that depends on the nature and extent of the focussing defect. The scattered light reaching a specific (ξ, η) point at the observation plane is no longer associated with a single $\mathbf{K}_j$ disturbance, but is an appropriately weighted sum of contributions

from a number of modes. As a result, the Bragg condition, eq. (77), is not strictly applicable in relating a particular (ξ, η) observation point to a specific plane-wave disturbance. The aberration or defocussing effect must be understood in detail before the measured intensity, or its time evolution may be used to infer the physical behavior of modes responsible for the scattering. Under defocussed conditions the spatial correlation function is also modified, though its functional form does retain a close resemblance to the intensity pattern associated with a single $\mathbf{K}_j$ diffraction "spot." In the following paragraphs we consider how the residual astigmatic blurring in the MK VI instrument affects the three slit-plane field properties enumerated in the opening paragraph.

3.3.1 Kinematic relations

To understand how the wave vector conservation criterion is to be applied at the slit plane of the present apparatus, we need to know (*i*) the slit-plane intensity pattern formed by scattering from a single plane-wave disturbance, and (*ii*) the relative positioning of the spots from the various allowed $\mathbf{K}_j$. In the MK VI instrument, the intensity pattern associated with a single $\mathbf{K}_j$ is identical to the diffraction- and aberration-affected instrumental profile whose properties were treated in detail in Sections 3.1 and 3.2. At the slit plane, therefore, the single $\mathbf{K}_j$ diffraction spots have the elongated gaussian shape depicted in Fig. 5. Expressed in terms of angular coordinates via eq. (79), the normalized intensity distribution within a "spot" is simply

$$\frac{I(\theta, \varphi)}{I(\theta_j, \varphi_j)} = \exp\left\{-\frac{(\theta - \theta_j)^2}{\delta\theta^2(1/e)}\right\} \exp\left\{-\frac{(\varphi - \varphi_j)^2}{\delta\varphi^2(1/e)}\right\}. \tag{80}$$

The reference point (θ_j, φ_j) specifies the angular position of the spot center, which, in the present case, is correctly predicted by the Bragg condition, eq. (77).

Given a correct form for the intensity distribution within a single $\mathbf{K}_j$ pattern, we must still determine the slit-plane spacing of the spots associated with the family of allowed $\mathbf{K}_j$. Clearly, this spacing depends on the reciprocal lattice of the orthonormal expansion functions $\exp(i\mathbf{K}_j \cdot \mathbf{r}')$ which, in turn, is fixed by the geometry of the scattering volume. For sufficiently small scattering angles, the actual three-dimensional scattering sample can be taken to be equivalent to a two-dimensional phase object placed normal to the incoming probe beam.[28] The scattering disturbances in this "phase-sheet" may be represented in terms of a two-dimensional plane-wave Fourier expansion

$$\sum_{K_x} \sum_{K_y} \cdots \exp(iK_x x) \exp(iK_y y),$$

with the (K_x, K_y) chosen to make the expansion functions orthonormal over the instrument's full aperture. For a rectangular aperture with full-width x and y dimensions b_x and b_y, the allowed $\mathbf{K}_j$ can be obtained from the cyclic boundary condition relations

$$K_x(m) = \frac{2\pi m}{b_x}, \qquad K_y(n) = \frac{2\pi n}{b_y}, \tag{81}$$

where m and n are the integers

$$m, n = 0, \pm 1, \pm 2, \cdots. \tag{82}$$

The scattering angles (θ_j, φ_j) for the central ray of the diffracted beam produced by a particular $\mathbf{K}(m, n)$ are then given by the small-angle Bragg conditions,

$$\begin{aligned} K_x(m) &= k_0\theta_m = \frac{2\pi m}{b_x} \\ K_y(n) &= k_0\varphi_n = \frac{2\pi n}{b_y}. \end{aligned} \tag{83}$$

It follows that the family of diffracted beams are brought to a focus at the slit plane on the vertices of a rectangular mesh whose grid spacings are given by

$$\xi_{SP} = f\theta_{SP} = f\left(\frac{\lambda_0}{b_x}\right) \tag{84}$$

$$\eta_{SP} = f\varphi_{SP} = f\left(\frac{\lambda_0}{b_y}\right). \tag{85}$$

For the MK VI instrument at full aperture ($b_x = 5.0$ cm, $b_y = 5.0$ cm), the equivalent angular mesh spacings are

$$\theta_{SP} = \varphi_{SP} = 10\ \mu\text{rad}. \tag{86}$$

If we imagine the instrumental profile contours of Fig. 5 arranged on such a mesh, there will be little overlap in the $\hat{\theta}$ direction but considerable overlap along $\hat{\varphi}$. The light received at some (θ, φ) point in the slit plane will contain contributions from roughly 10 distinct $\mathbf{K}(m, n)$, each having the same $m(K_x)$ index but differing $n(K_y)$ components. Because the MK VI instrument is capable of probing θ values so close to the diffraction limit, corresponding to a very small m index, $m = 5$–300, these multiple contributions can prove a serious problem. This point is illustrated in Fig. 19, which shows the $(1/e)$ contour of a single $\mathbf{K}(m, n)$ intensity pattern centered at $\theta = 80$ μrad, $\varphi = 0$ superimposed on the slit-plane mesh of the (θ_m, φ_n). The θ and φ axes of the figure can also be labelled in terms of the wave vector components K_x and K_y to which the angles are directly proportional as

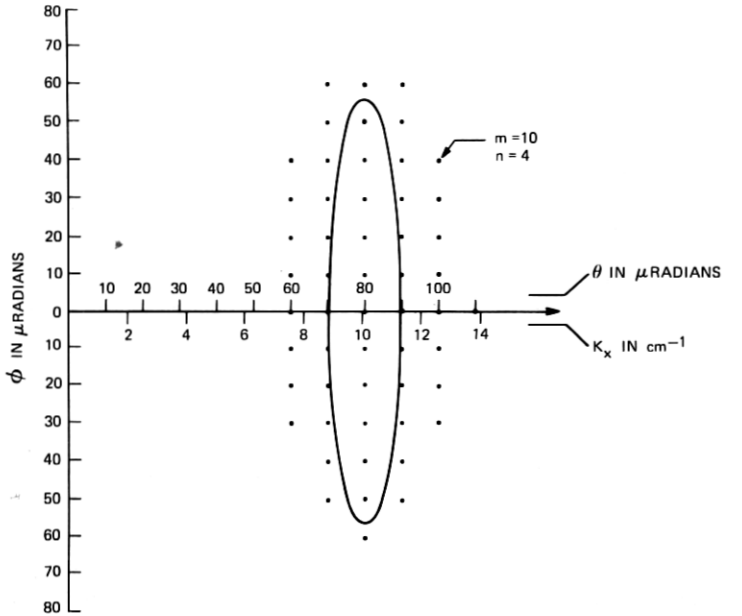

Fig. 19—Resolution function of the MK VI instrument superimposed on the slit-plane mesh points corresponding to the allowed scattering vectors $\mathbf{K}_j$.

indicated in eq. (83). For the eleven mesh points falling within the contour, the magnitude of the associated $\mathbf{K}(m, n)$ varies considerably. For the point at the center of the contour, we have ($m = 8$, $n = 0$) and

$$|\mathbf{K}| = 2\pi[(m/b_x)^2 + (n/b_y)^2]^{\frac{1}{2}} = 10.0 \text{ cm}^{-1},$$

while for the points at the φ extremes ($m = 8$, $n = 5$), we find

$$|\mathbf{K}| = 11.9 \text{ cm}^{-1}.$$

When the physical properties of the modes are strongly $|\mathbf{K}|$ dependent, this overlap can lead to a difficult task in the interpretation of the measured intensity and/or its time dependence.

Clearly, the $|\mathbf{K}|$ smearing effect becomes less significant as θ increases. Less obvious is the fact that the problem of multiple $\mathbf{K}_j$ contributions can be alleviated by stopping down the beam height of the instrument, b_y. As was pointed out in the conclusion of Section 3.2, the cylindrical distortion of the probe-beam wave fronts, which is a manifestation of the collimating mirror's astigmatism, can be made negligibly small by reducing b_y. With $b_y \leqq 0.5$ cm, for example, the beam incident on the sample can be considered as collimated to within the diffraction limit. In this case, the usual kinematic conditions apply in relation to the far-field scattered light; that is, the far-field array of

"spots" now form a contiguous and nonoverlapping pattern. Of course, each spot is elongated along $\hat{\varphi}$ by diffraction-spreading because of the imposed asymmetry of the probe-beam dimensions, i.e, $b_x = 5.0$ cm and $b_y \leqq 0.5$ cm, but the angular spot spacings $\theta_{SP} = (\lambda/b_x)$ and $\varphi_{SP} = (\lambda/b_y)$ are correspondingly asymmetric. Given this particular situation in the far field, we must still consider the effect of the astigmatism associated with the light-collecting mirror. As b_y is *decreased*, the $\hat{\varphi}$ direction astigmatic blurring at the slit plane is *decreased* proportionally,* while $\hat{\varphi}$ blurring due to diffraction increases. At some point, a crossover occurs beyond which diffraction spread dominates the slit-plane imaging. In this limit, the collecting mirror appears aberration free and the far-field pattern of $\mathbf{K}_j$ spots undergoes the normal one-to-one, no-overlap mapping onto the slit plane. For the MK VI configuration, the crossover occurs at $b_y \approx 0.5$ cm or roughly $\frac{1}{10}$ of the full design aperture height. Of course, it should be noted that under fully diffraction-limited conditions ($b_x = 5.0$ cm, $b_y < 0.5$ cm), the instrument retains its very asymmetric resolution profile. What we have done is to make the instrument appear to be in "good focus" by introducing a sufficient amount of φ direction diffraction spreading to swamp the aberration defocussing. The price paid for this is that the instrument becomes incapable of probing scattering disturbances having as long a $\hat{y}$ direction wavelength (that is as small a value of K_y) as can be resolved in the $\hat{x}$ direction.

3.3.2 Relation between the slit-plane intensity and the scattering cross-section of the sample

In the absence of aberrations or other defocussing problems, the far-field or observation plane scattered intensity can be related easily to the mean-square amplitude of the scattering perturbations using the standard integral expression for the scattered field.[1,3,27] In the presence of imaging aberrations, the total scattered power per plane-wave mode is unchanged; however, now the calculation of the slit-plane intensity is complicated by the overlap of the various $\mathbf{K}_j$ diffraction spots. For the MK VI instrument, a relation between the scattered power per mode and the observed slit-plane intensity may be obtained as follows.

The slit-plane intensity corresponding to a single $\mathbf{K}_j$ disturbance can be written down formally as

$$|E_{nm}(\theta, \varphi)|^2 = |E_{nm}(\theta_m, \varphi_n)|^2 \exp\left[-\frac{(\theta - \theta_m)^2}{\delta\theta^2(1/e)}\right] \exp\left[-\frac{(\varphi - \varphi_n)^2}{\delta\varphi^2(1/e)}\right] \quad (87)$$

with slit-plane position specified in angular units. The position of the

* See Figure 13 and the discussion pertaining to this figure.

central ray of the pattern (θ_m, φ_n) is given by eq. (83). The total scattered power in the single $\mathbf{K}_j$ pattern is just

$$P_s(\mathbf{K}_j) = \int\int d\theta d\varphi \, |E_{nm}(\theta, \varphi)|^2$$
$$= \pi\delta\theta(1/e)\delta\varphi(1/e)\,|E_{nm}(\theta_m, \varphi_n)|^2. \tag{88}$$

The problem now is to relate the observed total slit-plane intensity to the peak mode intensities, $|E_{nm}(\theta_m, \varphi_n)|^2$. The intensity observed at the position (θ, φ) is the sum over all possible mode contributions:

$$|E_s(\theta, \varphi)|^2$$
$$= \sum_{n,m} |E_{nm}(\theta_m, \varphi_n)|^2 \exp\left[-\frac{(\theta - \theta_m)^2}{\delta\theta^2(1/e)}\right] \exp\left[-\frac{(\varphi - \varphi_n)^2}{\delta\varphi^2(1/e)}\right]. \tag{89}$$

If $|E_{nm}(\theta_m, \varphi_n)|^2$ is independent of (n, m) over the range where the gaussian terms are nonvanishing, eq. (89) can be simplified to give

$$|E_s(\theta, \varphi)|^2 = |E_{nm}(\theta_m, \varphi_n)|^2 S_m S_n, \tag{90}$$

where S_m and S_n are the factored sums

$$S_m = \sum_m \exp - \{[\theta - m(\lambda_0/b_x)]^2/\delta\theta^2(1/e)\} \tag{91}$$

$$S_n = \sum_n \exp - \{[\varphi - n(\lambda_0/b_y)]^2/\delta\varphi^2(1/e)\}. \tag{92}$$

Consider the S_m sum expressed in the following dimensionless form

$$S_m = \sum_m \exp - \left\{\frac{\theta}{\delta\theta(1/e)} - m\left(\frac{\lambda}{b_x}\right)\frac{1}{\delta\theta(1/e)}\right\}^2$$
$$= \sum_m \exp\,(-[u - ma]^2), \tag{93}$$

where

$$u \equiv \frac{\theta}{\delta\theta(1/e)}, \qquad a \equiv \frac{1}{\delta\theta(1/e)}\frac{\lambda_0}{b_x}. \tag{94}$$

Although the indicated summation cannot be carried out explicitly, it can be expressed in a more useful form via the identity

$$\sum_m \exp\,[-(u - ma)^2] = \frac{\sqrt{\pi}}{a}\sum_m \exp\left(-\frac{m^2\pi^2}{a^2}\right)\cos\,(2m\pi u/a), \tag{95}$$

which is an immediate corollary of Poisson's formula.[38] Applying this identity to the S_m summation yields

$$S_m = \frac{\sqrt{\pi}\delta\theta(1/e)}{(\lambda/b_x)}\sum_m \exp\left[-\frac{m^2\pi^2\delta\theta^2(1/e)}{(\lambda/b_x)^2}\right]\cos\left[\frac{2m\pi\theta}{(\lambda/b_x)}\right]. \tag{96}$$

For the numerical parameters relevant to the MK VI instrument, $\delta\theta(1/e) = 9.6\ \mu\text{rad}$, $(\lambda/b_x) = 10\ \mu\text{rad}$, we need retain only the $m = 0$ term in the right-hand side of eq. (96). With an error less than 10^{-4}, we may take

$$S_m = \frac{\sqrt{\pi}\delta\theta(1/e)}{(\lambda/b_x)}. \tag{97}$$

A similar result follows easily for S_n. We then have for the total slit-plane intensity

$$|E_s(\theta, \varphi)|^2 = |E_{nm}(\theta_m, \varphi_n)|^2 \frac{\sqrt{\pi}\,\delta\theta(1/e)}{(\lambda/b_x)} \frac{\sqrt{\pi}\,\delta\varphi(1/e)}{(\lambda/b_y)}. \tag{98}$$

As this result shows, the various elongated gaussian patterns associated with the individual $\mathbf{K}_j$ modes overlap in the slit plane to produce an essentially uniform illumination.

The unknown intensity factors $|E_{nm}(\theta_m, \varphi_n)|^2$ can now be eliminated between eqs. (88) and (98) to give the desired relationship between the overall slit-plane intensity and the scattered power per mode, namely,

$$P_s(\mathbf{K}_j) = |E_s(\theta_j, \varphi_j)|^2(\lambda/b_x)(\lambda/b_y). \tag{99}$$

Equation (99) is the basic result which allows the measured intensity to be related quantitatively to the amplitudes of the individual scattering perturbations.*

Note that the power actually contained within the angular area of a single $\mathbf{K}_j$ pattern

$$|E_s(\theta_j, \varphi_j)|^2\delta\theta(1/e)\delta\varphi(1/e)$$

is larger than the scattered power per mode by the factor

$$\frac{\delta\theta(1/e)}{(\lambda/b_x)} \frac{\delta\varphi(1/e)}{(\lambda/b_y)}.$$

This ratio gives a rough gaussian weighted measure of the number of modes that contribute to the intensity reaching a particular (θ, φ).

3.3.3. The spatial coherence function of the slit-plane field

In light-scattering experiments designed to extract spectral information from the scattered field using photocurrent correlation techniques, the feasibility of a particular measurement is critically dependent on the range of transverse spatial correlation that characterizes the observation plane field.[2,3,27] The extent of the correlation is de-

* See the discussion which follows eq. (113) and leads to eq. (124).

scribed quantitatively by the normalized mutual coherence function[39,40]

$$T(\xi, \eta; \Delta\xi, \Delta\eta) = \frac{\langle \mathbf{E}_s(\xi, \eta; t) \cdot \mathbf{E}_s^*(\xi + \Delta\xi, \eta + \Delta\eta; t) \rangle}{\{\langle |\mathbf{E}_s(\xi, \eta; t)|^2 \rangle \langle |\mathbf{E}_s(\xi + \Delta\xi, \eta + \Delta\eta; t)|^2 \rangle\}^{\frac{1}{2}}}, \quad (100)$$

where (ξ, η) and $(\xi + \Delta\xi, \eta + \Delta\eta)$ are two arbitrary points in the observation plane. The angular brackets denote an appropriate ensemble or time average. The function $T(\cdots)$ reaches its maximum value, $T(\cdots) = 1$, for $\Delta\xi = \Delta\eta = 0$ and, in general, decreases smoothly to zero as $\Delta\xi$ and/or $\Delta\eta$ increase. The contour in $\Delta\xi$ and $\Delta\eta$ around (ξ, η) on which the coherence function reaches some specified numerical value may be taken as a measure of the area over which there is correlated temporal behavior of the two field amplitudes.

When the main probe beam is derived from a source having perfect transverse spatial coherence, as is the case here, then the presence of the spatial incoherence in the scattered field is totally attributable to the scattering processes taking place in the illuminated volume. The spatial coherence properties of the scattered field are uniquely determined at the exit face of the sample and are most easily specified analytically by calculating the mutual coherence function on a far-field reference sphere, 0, centered on the scattering volume. In purely formal terms, we can write

$$T_0(\mathbf{r}, \boldsymbol{\varrho}) = \frac{\langle \mathbf{E}_s(\mathbf{r}, t) \cdot \mathbf{E}_s^*(\mathbf{r} + \boldsymbol{\varrho}, t) \rangle}{\{\langle |\mathbf{E}_s(\mathbf{r}, t)|^2 \rangle \langle |\mathbf{E}_s(\mathbf{r} + \boldsymbol{\varrho}, t)|^2 \rangle\}^{\frac{1}{2}}}, \quad (101)$$

where $\mathbf{r}$ and $\mathbf{r} + \boldsymbol{\varrho}$ both terminate on the surface of the far-field sphere, 0. Generally speaking, $T_0(\mathbf{r}, \boldsymbol{\varrho})$ can be calculated in a straightforward fashion once it is assumed that the scattering perturbations satisfy certain basic stochastic criteria.

The relationship between the observation plane coherence function $T(\xi, \eta; \Delta\xi, \Delta\eta)$ and the far-field function $T_0(\mathbf{r}, \boldsymbol{\varrho})$ depends, of course, on the detailed characteristics of the optical system which collects and images the scattered light, and must include the effects of aberrations. There are two alternative procedures that may be used to obtain this relationship. The first involves the use of the plane wave $\mathbf{K}_j$ expansion of the scattering perturbations that was introduced in the beginning of this section. For the MK VI instrument, we have already calculated the slit-plane field produced by the scattering from the individual $\mathbf{K}_j$. In the notation of eq. (89), we have

$$\mathbf{E}_s(\xi, \eta; \mathbf{K}_j) = \mathbf{E}_{nm}(\xi_m, \eta_n) \exp\left[-\frac{(\xi - \xi_m)^2}{2f^2\delta\theta^2(1/e)} \right] \exp\left[-\frac{(\eta - \eta_n)^2}{2f^2\delta\varphi^2(1/e)} \right], \quad (102)$$

where f is the effective focal length of the light collection system. In

theory, therefore, we could calculate $T(\xi, \eta; \Delta\xi, \Delta\eta)$ directly by expressing the total slit-plane field as a sum over the $\mathbf{E}_s(\xi, \eta; \mathbf{K}_j)$ and then performing the statistical average indicated in eq. (100). In the absence of aberrations or other imaging defects, this direct method represents the simplest approach. For perfect imaging, the individual plane-wave scattered field patterns are essentially nonoverlapping at the observation plane and the coherence function is effectively dominated by the contribution of a single $\mathbf{K}_j$ term. However, when imaging errors produce a significant overlap of the $\mathbf{E}_s(\xi, \eta; \mathbf{K}_j)$ at the observation plane, as is the case for the present apparatus, then obtaining the analytical form of $T(\xi, \eta; \Delta\xi, \Delta\eta)$ by the direct method becomes a difficult mathematical problem.

The second alternative approach involves a direct calculation of the far-field coherence function $T_0(\mathbf{r}, \boldsymbol{\varrho})$ from which $T(\xi, \eta; \Delta\xi, \Delta\eta)$ is obtained by using the fundamental laws that govern the "propagation" of mutual coherence in an optical system. This latter method is generally the more useful when the light-collection system departs significantly from ideal imaging.

For the scattering angles relevant to the MK VI instrument, the two-dimensional "phase sheet" model of the scattering sample may be used to simplify the calculation of $T_0(\mathbf{r}, \boldsymbol{\varrho})$. For this two-dimensional model object, the reference sphere coherence function is given by the van Cittert-Zernike theorem[39] as

$$T_0(\theta, \varphi; \theta - \theta'; \varphi - \varphi') = \frac{2\pi \int_S \int dxdy\, |E_0(x, y)|^2 \exp\{ik_0[(\theta - \theta')x + (\varphi - \varphi')y]\}}{2\pi \int_S \int dxdy\, |E_0(x, y)|^2}, \quad (103)$$

where both $\mathbf{r}$ and $\boldsymbol{\varrho}$ have been expressed in the cartesian angular coordinates θ and φ. In eq. (103), the factor $|E_0(x, y)|^2$ is the illumination function of the object, in our case the "phase-sheet" sample. The surface integral is to be taken over the entire (x, y) plane or over the open aperture of the object, as appropriate. It should be noted that the van Cittert-Zernike theorem will hold as long as the perturbations in the scattering "phase sheet" have a correlation distance, which is short compared to the characteristic spatial dimensions of $|E_0(x, y)|^2$. This condition is, in general, well satisfied in the typical scattering experiment.

At small angles, where eq. (103) is valid, the far-field spatial coherence function is independent of the absolute angular position of either observation point and depends only on the separations $(\theta - \theta')$ and $(\varphi - \varphi')$. In terms of these difference variables, $T_0(\cdots)$ is just

the normalized Fourier transform of the source *intensity*. As such, it bears an extremely close resemblance to the instrumental profile calculated in Sections 3.1 and 3.2.

For the MK VI instrument, the illumination function is the gaussian

$$|E_0(x, y)|^2 = E_0^2 \exp\left(-\frac{x^2 + y^2}{\sigma^2}\right) \tag{104}$$

and we have from eq. (103)

$$T_0(\theta, \varphi; \theta - \theta', \varphi - \varphi') = \frac{\int_{-b_x/2}^{b_x/2} \exp(-x^2/\sigma^2) \exp[ik_0(\theta - \theta')x]dx}{\int_{-b_x/2}^{b_x/2} \exp(-x^2/\sigma^2)dx} \times \frac{\int_{-b_y/2}^{b_y/2} \exp(-y^2/\sigma^2) \exp[ik_0(\varphi - \varphi')y]dy}{\int_{-b_y/2}^{b_y/2} \exp(-y^2/\sigma^2)dy}, \tag{105}$$

where b_x and b_y are the aperture dimensions at the scattering sample. As is evident from eq. (105), the coherence function factors for the case of gaussian illumination and we can write

$$T_0(\theta, \varphi; \theta - \theta', \varphi - \varphi') = T_0'(\Delta\theta)T_0'(\Delta\varphi),$$

where $\Delta\theta = \theta - \theta'$ and $\Delta\varphi = \varphi - \varphi'$. The functions $T_0'(\Delta\theta)$ and $T_0'(\Delta\varphi)$ are given by the appropriate integrals in eq. (105). Each of these integrals is a finite domain Fourier transform of a gaussian kernel of the type considered in detail in Section 3.1 with respect to aperture apodization and vignetting. The only difference is that in eq. (105), the "intensity," $\exp(-x^2/\sigma^2)$, replaces the "field," $\exp(-x^2/2\sigma^2)$, which appeared in the diffraction calculations. It is not hard to show that the factored coherence functions $T_0'(\Delta\theta)$ and $T_0'(\Delta\phi)$ are identical to the normalized intensity profiles of Fig. 9 if one uses the correspondence

$$|T_0'(\psi)| = \frac{I(\psi/2)}{I(0)}. \tag{106}$$

Given the form of the far-field reference sphere function T_0, we must now determine the relationship between T_0 and the desired slit-plane correlation function.

One of the fundamental results of coherence theory is that second-order mutual coherence functions, such as $T(\cdots)$, propagate according to the wave equations as "field" variables. That is, once $T(\cdots)$ is specified on any surface in an optical system, its form on any other surface in the system may be found by treating the coherence function

as one would any electric field distribution. Therefore, all of the usual wave-diffraction and/or geometrical-optics approaches used to analyze wave-front propagation in an optical system are directly applicable to the coherence function.

For the MK VI apparatus, the coherence "field" described by T_0 is identical to the far-field electric field that describes the instrument's directly transmitted probe beam, except for a numerical change in the beam-width parameter σ. The effective beam width which characterizes the mutual coherence "field," σ_T, is related to the actual beam width of the instrument, σ^*, by the result

$$\sigma_T^2 = \frac{(\sigma^*)^2}{2}. \tag{107}$$

Except for this numerical change, the diffraction and aberration results of Sections 3.1 and 3.2 may be used intact to describe the slit-plane coherence function. In terms of angular coordinates at the slit and the widths $\delta\theta(1/e)$ and $\delta\varphi(1/e)$, which were used to characterize the instrumental profile, we have easily

$$\begin{aligned} T(\theta, \varphi; \theta - \theta', \varphi - \varphi') &= T'(\Delta\theta)T'(\Delta\varphi) \\ &= \exp\left\{-\frac{(\theta - \theta')^2}{4\delta\theta^2(1/e)}\right\} \exp\left\{-\frac{(\varphi - \varphi')^2}{4\delta\varphi^2(1/e)}\right\}. \end{aligned} \tag{108}$$

In the slit plane, as was the case on the surface of the far-field reference sphere, the slit-plane coherence functions are related to the intensity profile of the transmitted beam by the transformation

$$|T'(\psi)| = \frac{I(\psi/2)}{I(0)}.$$

Equation (108) is the basic result which may be used to evaluate the scattered or stray-light power-per-coherence region or estimate the number of coherence regions encompassed by a particular choice of main-slit size. For example, given the slit-plane scattered intensity $|E_s(\theta, \varphi)|^2$, we can form the weighted integral

$$\frac{dP_s(\theta, \varphi)}{d\Omega_{COH}} = \int\int d\theta' d\varphi' |E_s(\theta', \varphi')|^2 [T'(\theta - \theta')T'(\varphi - \varphi')]^2, \tag{109}$$

which is a useful measure of the power-per-coherence solid angle as measured at the slit.[2,3,27] In general, $|E_s(\theta', \varphi')|^2$ is slowly varying over the angular range where $[T'(\theta - \theta')T'(\varphi - \varphi')]^2$ is nonvanishing and can be removed from the integral to give

$$\frac{dP_s(\theta, \varphi)}{d\Omega_{COH}} = |E_s(\theta, \varphi)|^2 \overline{\Delta\theta}_{COH} \overline{\Delta\varphi}_{COH}, \tag{110}$$

where the mean full-width coherence angles, $\overline{\Delta\theta}_{COH}$ and $\overline{\Delta\varphi}_{COH}$, are defined by the integrals

$$\begin{aligned}\Omega_{COH} &= \overline{\Delta\theta}_{COH}\overline{\Delta\varphi}_{COH} \\ &= \int [T'(\Delta\theta)]^2 d(\Delta\theta) \int [T'(\Delta\varphi)]^2 d(\Delta\varphi).\end{aligned} \tag{111}$$

Combining eqs. (108) and (109) gives for the MK VI instrument

$$\begin{aligned}\overline{\Delta\theta}_{COH} &= \sqrt{2\pi}\delta\theta(1/e) = 24.1\ \mu\text{rad} \\ \overline{\Delta\varphi}_{COH} &= \sqrt{2\pi}\delta\varphi(1/e) = 140.4\ \mu\text{rad}\end{aligned} \tag{112}$$

and eq. (110) becomes

$$\frac{dP_s(\theta, \varphi)}{d\Omega_{COH}} = |E_s(\theta, \varphi)|^2 \sqrt{2\pi}\delta\theta(1/e)\sqrt{2\pi}\delta\varphi(1/e). \tag{113}$$

Earlier in this section, we obtained an expression for $|E_s(\theta, \varphi)|^2$ based on a plane-wave-mode expansion of the scattering perturbations. That result may be used in eq. (113) to yield a relationship between the observed scattered power-per-coherence solid angle and the scattered power-per-$\mathbf{K}_j$ mode. From eqs. (99) and (113), we find

$$\frac{dP_s(\theta_j, \varphi_j)}{d\Omega_{COH}} = \frac{\sqrt{2\pi}\delta\theta(1/e)}{(\lambda/b_x)} \times \frac{\sqrt{2\pi}\delta\varphi(1/e)}{(\lambda/b_y)} P_s(\mathbf{K}_j). \tag{114}$$

The product of the correction factors

$$\frac{\sqrt{2\pi}\delta\theta(1/e)}{(\lambda/b_x)} \times \frac{\sqrt{2\pi}\delta\varphi(1/e)}{(\lambda/b_y)}$$

is a rough measure of the number of modes that contribute to the power observed in a single coherence region at the slit plane, while the individual terms indicate the extent of the multiple mode contribution in the $\hat{\theta}$ and $\hat{\varphi}$ directions. For the MK VI instrument at full aperture, the numerical values of the correction factors are

$$\begin{aligned}\frac{\sqrt{2\pi}\ \delta\theta(1/e)}{(\lambda/b_x)} &= 2.4 \\ \frac{\sqrt{2\pi}\ \delta\varphi(1/e)}{(\lambda/b_y)} &= 14.0.\end{aligned} \tag{115}$$

The results given in eqs. (99), (113), and (114) together with the known form of the instrumental profile may be combined in various ways to calculate normalized scattering cross sections from measured slit-plane intensities. One important calculation of this type is to express the observed stray-light levels in the MK VI apparatus in

terms of an equivalent scattering cross section. For the experimental profile curves shown in Fig. 4, we may write down an analytical expression for the measured stray-light photocurrent, $i(\theta)$, as

$$i(\theta) = \alpha \int_{-\Delta\theta_{SL}/2}^{\Delta\theta_{SL}/2} \int_{-\Delta\varphi_{SL}/2}^{\Delta\varphi_{SL}/2} |E_{st}(\theta, \varphi)|^2 d\theta d\varphi, \tag{116}$$

where $|E_{st}(\theta, \varphi)|^2$ is the stray-light intensity at the slit plane and $\Delta\theta_{SL}$ and $\Delta\varphi_{SL}$ specify the full-width slit dimensions in angular units. The proportionality factor α relates the photocurrent to the optical power passed by the slit and includes the detector quantum efficiency, light-collection losses, etc. If the intensity $|E_{st}(\theta, \varphi)|^2$ is relatively constant over the slit aperture, we have simply

$$i(\theta) = \alpha |E_{st}(\theta, 0)|^2 \Delta\theta_{SL} \Delta\varphi_{SL}, \tag{117}$$

where we have assumed that $\Delta\varphi_{SL}$ is situated symmetrically around $\varphi = 0$. Combining this result with eq. (110) gives the relation between the measured photocurrent and the stray-light power-per-coherence solid angle as

$$i(\theta) = \alpha \frac{dP_{st}(\theta, 0)}{d\Omega_{COH}} \frac{\Delta\theta_{SL}}{\overline{\Delta\theta}_{COH}} \frac{\Delta\varphi_{SL}}{\overline{\Delta\varphi}_{COH}}. \tag{118}$$

To eliminate the unknown proportionality constant α, we make use of photocurrent observed at $\theta = 0$, the peak of the directly transmitted beam. Given the normalized slit-plane intensity profile of the direct beam, $I(\theta, \varphi)/I(0, 0)$, we can calculate the fraction of the total beam power, P_0, passed by the slit at $\theta = 0$ as

$$\frac{\int_{-\Delta\theta_{SL}/2}^{\Delta\theta_{SL}/2} \int_{-\Delta\varphi_{SL}/2}^{\Delta\varphi_{SL}/2} \frac{I(\theta, \varphi)}{I(0, 0)} d\theta d\varphi}{\iint_{\text{all } \Omega} \frac{I(\theta, \varphi)}{I(0, 0)} d\theta d\varphi} \equiv \gamma, \tag{119}$$

where for the MK VI apparatus we have

$$\frac{I(\theta, \varphi)}{I(0, 0)} = \exp\left[- \frac{\theta^2}{\delta\theta^2(1/e)} \right] \exp\left[- \frac{\varphi^2}{\delta\varphi^2(1/e)} \right].$$

The numerical value of the error function integrals in eq. (119) could be obtained from tabulated results for particular values of $\Delta\theta_{SL}$ and $\Delta\varphi_{SL}$; however, in the present case where the slit dimensions satisfy the inequalities

$$\begin{aligned} \Delta\theta_{SL} &\ll \delta\theta(1/e) \\ \Delta\varphi_{SL} &\gg \delta\varphi(1/e), \end{aligned} \tag{120}$$

we have the more useful analytical result

$$\gamma \cong \frac{\Delta\theta_{SL}}{\sqrt{\pi}\delta\theta(1/e)}. \tag{121}$$

The measured peak photocurrent, $i(0)$, is then

$$i(0) = \alpha P_0 \frac{\Delta\theta_{SL}}{\sqrt{\pi}\delta\theta(1/e)}. \tag{122}$$

Dividing eq. (118) by eq. (122) gives the useful result

$$\frac{i(\theta)}{i(0)} = \frac{1}{P_0}\frac{dP_{sl}(\theta, 0)}{d\Omega_{COH}}\frac{1}{\sqrt{2}}\frac{\Delta\varphi_{SL}}{\overline{\Delta\varphi_{COH}}}. \tag{123}$$

If desired, the quantity $dP_{sl}(\theta, 0)/d\Omega_{COH}$ can be replaced with the stray-light power per mode, $P_{sl}(K_j)$, by using eq. (114). This gives the very useful relationship

$$\frac{i(\theta)}{i(0)} = \frac{\mathcal{P}_{sl}(\mathbf{K}_j)}{\mathcal{P}_0}\frac{\sqrt{2\pi}\,\delta\theta(1/e)}{(\lambda/b_x)}\frac{\Delta\varphi_{SL}}{(\lambda/b_y)}. \tag{124}$$

IV. EMPIRICAL OBSERVATIONS ON THE STRAY-LIGHT BEHAVIOR OF OPTICAL ELEMENTS AT VERY SMALL ANGLES

Very little information of a quantitative nature is available concerning the imperfection scattering of optical elements at very small angles. As a result, the design and testing process leading to the present VSA instrument involved a significant amount of trial and error evaluation of various optical systems in a search for the desired stray-light performance. During this process, a certain amount of empirical information was obtained relating to the imperfection-scattering question. This section presents a brief discussion of these observations and their influence on the configuration adopted for the MK VI instrument.

4.1 Reflecting versus refracting optics

It is clear from a comparison of Figs. 1 and 6 that the implementation of a VSA scattering instrument using lenses would be significantly less involved than the MK VI off-axis mirror arrangement. The refracting system also has the advantage of strictly zero off-axis aberrations (coma, astigmatism, and distortion), although a "best form" single-element lens does have eight times the spherical aberration of an equivalent spherical mirror.[37] In fact, the earliest version of the present apparatus utilized precisely the kind of "straight-through" lens system illustrated in Fig. 6. This arrangement was abandoned because of

two problems:

(*i*) The presence of Newton's interference fringes crossing the illuminated field.
(*ii*) An excessive stray-light background.

The first problem arises because of the partial reflectivity of the two lens surfaces and can be solved to some extent through the use of antireflection (AR) coatings. However, even the best antireflection coated lens will form far-field Newton fringes with an integrated intensity of about $\frac{1}{4}$ percent of the incident beam power. This fact makes the refracting components generally unacceptable in a VSA system. The presence of these extraneous reflections and their associated interference fringes creates an intense fixed-pattern nuisance background which can make it impossible to observe the angular dependence of the sample scattered light. The stray-light background problem is a manifestation of small-angle scattering at the lens which may originate from three possible sources:

(*i*) Lens surface "roughness" or nonconformity (at least two surfaces).
(*ii*) Index of refraction inhomogeneity in the lens bulk material.
(*iii*) AR coating thickness nonuniformity (at least two surfaces).

By way of comparison, the possible sources of imperfection scattering from a first-surface reflector are

(*i*) Mirror surface "roughness" or nonconformity (one surface).
(*ii*) Reflective coating(s) thickness nonuniformity.
(*iii*) Reflective coating reflectivity nonuniformity.

From a theoretical standpoint, one should be able to evaluate the seriousness of each of these defects *a priori* by calculating the surface and/or bulk inhomogeneity scattering. This calculation is straightforward if one has available the spatial form of the roughness in terms of the spatial correlation function and the rms roughness amplitude. The effect of roughness or inhomogeneity is to impose a spatially random-phase perturbation in the optical path. The scattering that takes place as a result of this perturbation can be calculated via the same "phase-object" approach which is used for the primary scattering sample (see Section 2.6). The stray-light intensity observed at some specified scattering angles θ and φ is given by the Fourier transform of the roughness correlation function at a wave vector $|\mathbf{K}| = 2\pi/\Lambda$ satisfying the appropriate small-angle kinematic conditions. Unfortunately, the roughness wavelengths corresponding to the angular range of interest here (10^{-3} cm $\lesssim \Lambda \lesssim 1$ cm) are determined by a

spatial region of the roughness correlation function about which very little is presently known. This wavelength regime presents difficult measurement problems and is generally not probed by conventional roughness-testing techniques. The data that is available comes from two measurement techniques that tend to flank this regime on the short and long wavelength sides:

(*i*) The FECO* interferometer and allied methods[41,42] that exhibit good surface deviation resolution, 1 Å to 10 Å, but are useful only at short wavelengths ($\Lambda \lesssim 1000$ Å).

(*ii*) Conventional "surface-conformity" techniques such as the Foucault knife-edge and Twyman-Green interferometer tests that are useful primarily at longer roughness wavelengths (0.1 cm to 100 cm) and which exhibit relatively poor surface deviation resolution (50 Å $\rightarrow$ 2000 Å).

The stray-light measurements that were made during the course of the evolution of the present instrument provided the most sensitive roughness and inhomogeneity test for this awkward wavelength range. It was found experimentally that, for lenses and mirrors of the same fraction of the "state-of-the-art," the stray-light level of a refracting instrument was roughly 20 times that of its reflecting counterpart. In neither case did the VSA stray-light level correlate well with known short wavelength roughness and inhomogeneity data. Both types of components exhibited a spatial roughness spectrum that was strongly enhanced at long wavelengths. This enhancement did not appear to depend as strongly on the "surface-figure" of the component as one might be led to expect by qualitative theoretical arguments.

Comparisons were also made between mirror components having multilayer dielectric coatings and those with a conventional SiO-protected aluminized surface. The aluminized coatings can suffer from a spatially varying reflectivity caused by surface oxidation while high-reflectivity dielectric films tend to have a significantly smaller reflectivity modulation. However, the stray-light measurements showed no significant difference between the two types of coatings on similar "quality" substrates. Apparently the cumulative roughness of the greater number of dielectric layers offsets the dielectric coating's potential advantage.

4.2 Main scanning slit

Another major contributor to the stray-light level in earlier versions of the MK VI apparatus was the main angle-scanning slit. The slit selected for this application is a commercial Spex unit normally used

* Fringes of Equal Chromatic Order.

as an intermediate or exit slit on a double-grating spectrometer known for its low stray-light background. This fact not withstanding, severe stray-light problems were encountered in predecessors of the MK VI that had this slit located directly at the focal plane of the collecting mirror (mirror M_6 shown in Fig. 1). The origin of this problem was traced to scattering of the direct beam by the beveled surfaces of the slit jaws and to quasi-specular reflection from the slightly flattened and rounded jaw edges. This source of background by itself was of sufficient intensity to completely swamp the sum total of all other stray-light sources in the instrument.

This problem was solved in the MK VI apparatus by occulting the directly transmitted beam, before it reached the main scanning slit, with a precision knife-edge fabricated of highly attenuating black glass plate. The use of glass instead of metal permits the edge defining surfaces to be optically polished without cold flaw and rounding. In addition, the included angle formed by the edge surfaces is made obtuse, rather than the acute angle normally used, to avoid the feathering problems and surface irregularity enhancement associated with small included angles. The salient geometrical features of the knife-edge are illustrated in Fig. 20. The actual occulting edge is formed by a single beveling operation on polished flat stock and is oriented in use such that an incoming ray strikes the beveled face at the quasi-Brewster angle. The beveling angle is chosen so that the ray which is refracted into the plate travels parallel to the plate surfaces and is totally absorbed.

The improvement in stray-light level obtained by using the knife-edge to occult the direct beam, rather than relying solely on the main scanning slit, can be seen in Figs. 3 and 4. The improvement amounts to roughly an order of magnitude over the angular range of interest.

4.3 Aberration corrections and stray light

The reader familiar with optical system design will realize that the aberrations present in the MK VI instrument could be "corrected" using well-known techniques. However, the application of these correction methods has two drawbacks: cost and reduced stray-light performance. The simplest corrective measures, those which add the fewest number of optical elements to the basic apparatus, entail the use of off-axis fabricated, aspheric reflecting and/or refracting elements. These types of elements are, in general, exceedingly costly to fabricate. More sophisticated aberration-corrective designs, utilizing only spherical optics, require a larger number of additional elements. In either case, of course, the presence of additional optical surfaces means degraded stray-light performance. Furthermore, any corrective design

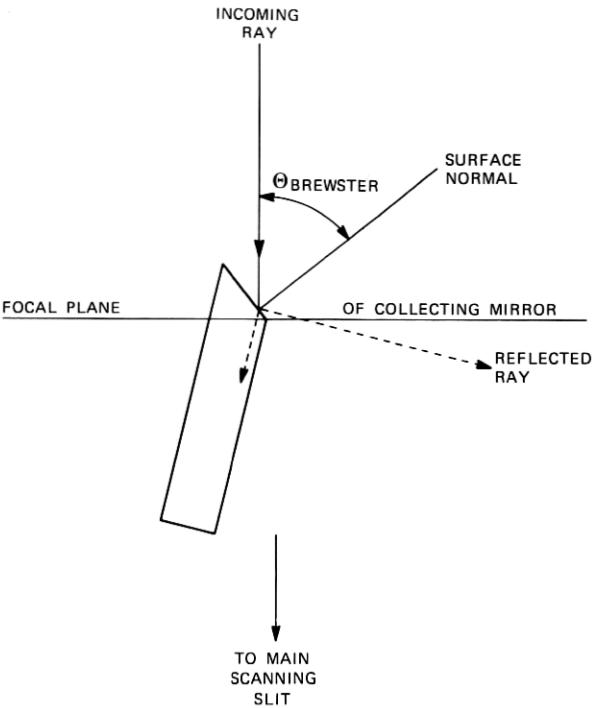

Fig. 20—Geometrical features of the occulting knife-edge used in the MK VI apparatus.

relying on the use of refracting elements will be further penalized by the excessive small-angle stray light which these elements generate.

APPENDIX A

Finite Slit-Width Effects in the Scanning of Gaussian Intensity Profiles

When a gaussian focal-plane profile is scanned by a finite-width slit, the transmitted power is proportional to the integral

$$J(\xi_0, \Delta) = \int_{\xi_0-\Delta}^{\xi_0+\Delta} \exp\left[-\xi^2/\delta\xi^2(1/e)\right]d\xi, \tag{125}$$

where ξ_0 gives the position of the center of a slit whose width is 2Δ. By writing the spatial coordinate ξ as

$$\xi = \xi_0 + \zeta \tag{126}$$

and making a change of variable, we may put eq. (125) into the form

$$J(\xi_0, \Delta) = \exp\left[-\xi_0^2/\delta\xi^2(1/e)\right] \times \int_{-\Delta}^{\Delta} \exp\left[-(2\xi_0 + \zeta^2)/\delta\xi^2(1/e)\right]d\zeta. \tag{127}$$

Table IX — Angular displacement, θ_0, at which an unbroadened gaussian and a slit-broadened gaussian reach specified fractions of peak intensity

$\frac{J(\theta_0, \Delta)}{J(0, \Delta)}$	θ_0 Unbroadened $\Delta_\theta = 0$ μrad (μrad)	θ_0 Slit Broadened $\Delta_\theta = 1$ μrad (μrad)	% Increase
1	0	0	—
1/2	7.993	8.022	0.36
$1/e$	9.600	9.635	0.36
10^{-1}	14.567	14.620	0.36
10^{-2}	20.601	20.675	0.36
10^{-3}	25.231	25.322	0.36
10^{-4}	29.135	29.239	0.36
10^{-5}	32.573	32.690	0.36
10^{-6}	35.682	35.810	0.36
10^{-7}	38.541	38.678	0.36
10^{-8}	41.203	41.348	0.36

For reasonably small values of the ratio $[\Delta/\delta\xi(1/e)]$, the gaussian term in the integrand of eq. (127) may be approximated by the leading term in its Taylor's series expansion

$$\exp\left[-\zeta^2/\delta\xi^2(1/e)\right] = 1 - \frac{\zeta^2}{\delta\xi^2(1/e)} + \cdots,$$

with a maximum error $\exp\left[-\Delta^2/\delta\xi^2(1/e)\right]$. Within this approximation, the remaining integral can be calculated in a straightforward manner to give

$$J(\xi_0, \Delta) = (2\Delta)\exp\left[-\xi_0^2/2\delta\xi^2(1/e)\right]\left\{\frac{\sinh\left[2\xi_0\Delta/\delta\xi^2(1/e)\right]}{\left[2\xi_0\Delta/\delta\xi^2(1/e)\right]}\right\}. \quad (128)$$

Since the function $(\sinh x)/x$ tends to unity as x goes to zero, the normalized slit-broadened profile is

$$\frac{J(\xi_0, \Delta)}{J(0, \Delta)} = \exp\left[-\xi_0^2/\delta\xi^2(1/e)\right]\left\{\frac{\sinh\left[2\xi_0\Delta/\delta\xi^2(1/e)\right]}{\left[2\xi_0\Delta/\delta\xi^2(1/e)\right]}\right\} \quad (129)$$

or its equivalent written in terms of the scattering angle $\theta = \xi/f$. Clearly, in the limit $\Delta \to 0$, eq. (129) describes the correct unbroadened gaussian. For $\Delta \neq 0$, the principal effect of the $(\sinh x)/x$ correction term is to push up the tails of the profile while leaving the peak of the gaussian relatively unaffected. A good quantitative feeling for the nature of this correction may be obtained by solving for the off-zero displacements, ξ_0, at which the broadened and unbroadened profiles reach specified fractions of their peak intensity. These ξ_0 values then specify the profile half-widths at the corresponding intensity level.

For the curves presented in Section II, the relevant numerical parameters, expressed in angular units, are:

$$\delta\theta(1/e) = (1/f)\delta\xi(1/e) = 9.6\ \mu\text{rad}$$
$$\Delta_\theta = (1/f)\Delta \qquad = 1.0\ \mu\text{rad}.$$

Table IX gives the calculated half-width values $\theta_0 = (\xi_0/f)$ obtained from eq. (129) for various choices of the ratio $J(\theta_0, \Delta)/J(0, \Delta)$. For comparison, the table also lists the corresponding half-widths of the uncorrected gaussian, and the percentage of line-width increase caused by the slit-width correction. As is evident from these results, the effect of the $(1/x)$ sinh x correction term is to alter the gaussian profile in such a way that the observed half-widths are an essentially constant *percentage* larger than the true values.

APPENDIX B

Numerical Evaluation of the Diffraction Profile of Apertured Gaussian Illumination

Equation (47) gives the basic integral for the truncated gaussian diffraction profile as

$$E(\xi) = \frac{E_0}{(f\lambda_0)^{\frac{1}{2}}} \int_{-b/2}^{b/2} \exp(-x^2/\sigma^2) \exp[i(2\pi/f\lambda_0)\xi x]dx. \quad (130)$$

This expression may be put into a form more suited to numerical computation as follows. We write the exp $i(\cdots)$ term as

$$\exp[i(2\pi/f\lambda_0)\xi x] = \cos Kx + i \sin Kx$$

with

$$K \equiv \frac{2\pi\xi}{f\lambda_0} = \frac{2\pi\theta}{\lambda_0} \quad (131)$$

and note that the sin Kx integral vanishes by symmetry. Next by a change of variable

$$x = \frac{bw}{2}, \quad (132)$$

we obtain

$$E(\xi) = \frac{bE_0}{(f\lambda_0)^{\frac{1}{2}}} \int_{w=0}^{w=1} \cos cw \exp(-a^2w^2)dw, \quad (133)$$

where a and c are defined as

$$c \equiv \frac{Kb}{2} = \left(\frac{2\pi\xi}{f\lambda_0}\right)\frac{b}{2} = \frac{\pi b\theta}{\lambda_0}, \qquad a^2 = \frac{b^2}{8\sigma^2}. \quad (134)$$

The gaussian in the integrand is now expressed in terms of its Taylor's

series expansion

$$\exp(-a^2x^2) = \sum_{n=0}^{\infty} \frac{(-1)^n(a^2x^2)^n}{n!}$$

to give $E(\xi)$ as

$$E(\xi) = \frac{bE_0}{(f\lambda_0)^{\frac{1}{2}}} \sum_{n=0}^{\infty} \frac{(-1)^n(a^2)^n}{n!} \int_{w=0}^{1} w^{2n} \cos(cw)\, dw. \tag{135}$$

Equation (135) forms the basis for the numerical computation of the profiles.

A simple closed-function form for the w integrals in eq. (135) does not exist; however, recursive relations among these integrals can be found from the standard integrals

$$\int_0^1 x^m \cos cx\, dx = \frac{\sin c}{c} - \frac{m}{c} \int_0^1 x^{m-1} \sin cx\, dx \tag{136}$$

and

$$\int_0^1 x^{m-1} \sin cx\, dx = -\frac{\cos c}{c} + \frac{(m+1)}{c} \int_0^1 x^{m-2} \cos cx\, dx. \tag{137}$$

Defining

$$L_m(c) \equiv \int_0^1 x^m \cos cx\, dx, \tag{138}$$

we easily obtain the following recursion formulae from eqs. (136) and (137):

$$(m+3)L_{m+2}(c) = \left(\frac{m+3}{c}\right) \sin c + \frac{(m+3)(m+2)}{c^2} \cos c - \frac{(m+3)(m+2)}{c^2} [(m+1)L_m(c)] \tag{139}$$

$$(m-1)L_{m-2}(c) = \left(\frac{c}{m}\right) \sin c + \cos c - \frac{c^2}{m(m+1)} [(m+1)L_m(c)]. \tag{140}$$

From eq. (136), we also have for $m = 0$

$$L_0(c) = \frac{\sin c}{c}. \tag{141}$$

In terms of the $L_m(c)$, the expression for the diffracted field takes the series form

$$E(\xi) = \frac{bE_0}{(f\lambda_0)^{\frac{1}{2}}} \sum_{n=0}^{\infty} \frac{(-1)^n(a^2)^n L_{2n}(c)}{n!} \tag{142}$$

and the desired normalized intensity profile is

$$\frac{I(\xi)}{I(0)} = \frac{\left\{ \sum_{n=0}^{\infty} \frac{(-1)^n (a^2)^n L_{2n}(c)}{n!} \right\}^2}{\left\{ \sum_{n=0}^{\infty} \frac{(-1)^n (a^2)^n L_{2n}(0)}{n!} \right\}^2}. \tag{143}$$

The zero argument L_m's can be written down explicitly from eq. (138), *viz.*

$$L_m(0) = \frac{1}{m+1}. \tag{144}$$

For the numerical results reported here, the series in eq. (143) were truncated at some $n = n_{MAX}$ by testing the value of $(1/n!)(a^2)^n L_{2n}(0)$ and terminating when this quantity was smaller than some chosen convergence criterion, ϵ. In the present case, ϵ was set at $\epsilon = 10^{-12}$. For the largest (b/σ) value, $(b/\sigma) = 8.33$, where the gaussian kernel of eq. (133) is

$$\exp(-a^2 w^2) = \exp(-8.68 w^2),$$

49 terms in the series were required for convergence.

For each individual pair of values for c and n_{MAX}, the required string of L_m's are generated by two subroutine programs.

B.1 Subroutine No. 1, $c < 1$

When the quantity $c = (Kb/2)$ is less than one, the L_m's are obtained by the following procedure.

(*i*) Calculate $L_m(c)$ for $m = 2n_{MAX}$ directly from the defining equation (138), using the Taylor expansion for $\cos cx$ to write

$$\begin{aligned} L_m(c) &= \sum_{n=0}^{\infty} \frac{(-1)^n c^{2n}}{(2n)!} \int_0^1 W^{2n+m} dW \\ &= \sum_{n=0}^{\infty} \frac{(-1)^n c^{2n}}{(2n)!(m+2n+1)}. \end{aligned} \tag{145}$$

(*ii*) Truncate the sum in eq. (145) when $c^{2n}/(2n)!(m+2n+1)$ is less than 10^{-12}.

(*iii*) Use this result for $L_{n_{MAX}}(c)$ to obtain the required L_m's *via* the backward recursion formula, eq. (140).

B.2 Subroutine No. 2, $c > 1$

When the quantity $c = (Kb/2)$ is greater than 1, the L_m's are found by a two-part procedure that depends on the value of n_{MAX}.

(*i*) For $m = 2n$ values for which the inequality $m = 2n < c$ is satisfied, use $L_1(c) = (\sin c)/c$ and the forward recursion rela-

tion, eq. (140). If $2n_{MAX}$ is less than c this first step gives all required L_m's.

(*ii*) If $2n_{MAX}$ is greater than c, set

$$L_m(c) \approx \frac{\cos c}{m+1}$$

for some $m \gg 2n_{MAX}$ and work backward using recursion relation eq. (140). The calculated string of L_m's is joined onto the forward recursion values from step (*i*) for some $m \approx c$ and then renormalized.

This rather elaborate procedure for calculating the L_m's is made necessary by the rapid accumulation of numerical round-off errors which arise in the repetitive application of the basic recursion formulae.

REFERENCES

1. I. L. Fabelinskii, *Molecular Scattering of Light*, New York: Plenum Press, 1968, Chapter III, pp. 155–246.
2. H. Z. Cummins and H. L. Swinney, "Light Beating Spectroscopy," in *Progress in Optics*, Vol. VIII, Emil Wolf, ed., Amsterdam, Netherlands: North Holland Publishing, 1970, pp. 135–200.
3. B. Chu, *Laser Light Scattering*, New York: Academic Press, 1974, Chapters IV–VII, IX, and X.
4. *Small Angle X-Ray Scattering*, H. Brumberger, ed., Proc. of Conf. at Syracuse University, June 24–26, 1965; sponsored by American Crystallographic Society, the Army Research Office, the National Science Foundation, and the University of Syracuse; New York: Gordon and Breach, 1967.
5. A. J. Renouprez, "Diffusion des Rayons X aux Petits Angle," *International Union of Crystallography, Commission on Crystallographic Apparatus*, Bibliography *4*, 1970, pp. 19–24.
6. W. H. Aughey and F. J. Baum, "Angular Dependence Light Scattering—A High Resolution Recording Instrument for the Angular Range 0.05°–140°," J. Opt. Soc. Amer. *44*, No. 11 (November 1954), pp. 833–837.
7. C. H. Henry and J. J. Hopfield, "Raman Scattering by Polaritons," Phys. Rev. Lett. *15*, No. 25 (December 1965), pp. 964–966.
8. S. P. S. Porto, B. Tell, and T. C. Damen, "Near Forward Raman Scattering in Zinc Oxide," Phys. Rev. Lett., *16*, No. 11 (March 1966), pp. 450–452.
9. J. B. Lastovka and G. B. Benedek, "Spectrum of Light Scattered Quasielastically from a Normal Liquid," Phys. Rev. Lett., *17*, No. 20 (November 1966), pp. 1039–1042.
10. J. B. Lastovka and G. B. Benedek, "Light Beating Techniques for the Study of the Rayleigh-Brillouin Spectrum," in *Physics of Quantum Electronics*, P. L. Kelly, B. Lax, and P. E. Tannenwald, eds., Proceedings of the Physics of Quantum Electronics Conference, San Juan, Puerto Rico, June 28–30, 1965, sponsored by the Office of Naval Research, New York: McGraw-Hill, 1966, pp. 231–240.
11. D. Eden and H. L. Swinney, "Optical Heterodyne Studies of Brillouin Scattering in Xenon Near the Critical Point," Opt. Commun., *10*, No. 2 (February 1974), pp. 191–194.
12. S. Chandrasekhar, *Hydrodynamic and Hydromagnetic Stability*, London: Oxford University Press, 1961.
13. V. M. Zaitsev and M. I. Shliomis, "Hydrodynamic Fluctuations Near the Convection Threshold," Zh. Eksp. Teor. Fiz., *59*, No. 5 (November 1970), pp. 1583–1592 [Sov. Phys. JEPT, *32*, No. 5 (May 1971), pp. 866–870].
14. R. Graham, "Generalized Thermodynamic Potential for the Convection Instability," Phys. Rev. Lett., *31*, No. 25 (December 1973), pp. 1479–1482.
15. M. G. Velarde, in *Hydrodynamics*, Proc. of the 1973 session of the École d'été de Physique Théorique, Les Houches, R. Balian, ed., New York: Gordon and Breach, in press.

16. P. Bergé and M. Dubois, "Convective Velocity Field in the Rayleigh-Bénard Instability: Experimental Results," Phys. Rev. Lett., *32*, No. 19 (May 1974), pp. 1041–1044.
17. W. A. Smith, "Temporal Correlations Near the Convection Instability Threshold," Phys. Rev. Lett., *32*, No. 21 (May 1974), pp. 1164–1167.
18. R. Farhadieh and R. S. Tankin, "Interferometric Study of Two-Dimensional Bénard Convection Cells," J. Fluid Mech., *66*, No. 4 (December 1974), pp. 739–752.
19. H. N. W. Lekkerkerker and J.-P. Boon, "Hydrodynamic Modes and Light Scattering Near the Convective Instability," Phys. Rev., A*10*, No. 4 (October 1974), pp. 1355–1360.
20. G. Ahlers, "Low Temperature Studies of the Rayleigh-Bénard Instability and Turbulence," Phys. Rev. Lett., *33*, No. 20 (November 1974), pp. 1185–1188.
21. J. B. McLaughlin and P. C. Martin, "Transition to Turbulence of a Statically Stressed Fluid," Phys. Rev. Lett., *33*, No. 20 (November 1974), pp. 1189–1192.
22. J. P. Gollub and M. H. Freilich, "Optical Heterodyne Study of the Taylor Instability in a Rotating Fluid," Phys. Rev. Lett., *33*, No. 25 (December 1974), pp. 1465–1468.
23. R. Graham, "Hydrodynamic Fluctuations Near the Convection Instability," Phys. Rev., A*10*, No. 5 (November 1974), pp. 1762–1784.
24. E. Guyon and P. Pieranski, "Convective Instabilities in Nematic Liquid Crystals," Physica (Utrecht), *73*, No. 1 (April 1974), pp. 184–194.
25. H. B. Möller and T. Riste, "Neutron-Scattering Study of Transitions to Convection and Turbulence in Nematic Para-azoxyanisole," Phys. Rev. Lett., *34*, No. 16 (April 1975), pp. 996–999.
26. *Fluctuations, Instabilities, and Phase Transitions*, T. Riste, ed., Proceedings of the NATO Advanced Study Institute, Geilo, Norway, April 11–20, 1975, New York: Plenum Press, 1975.
27. J. B. Lastovka, "Light Mixing Spectroscopy and the Spectrum of Light Scattered by Thermal Fluctuations in Liquids," Ph.D. Thesis, Massachusetts Institute of Technology, 1967, Chapter III, pp. 156–357.
28. J. B. Lastovka, unpublished paper.
29. F. A. Jenkins and H. E. White, *Fundamentals of Optics*, 3rd ed., New York: McGraw-Hill, 1957, pp. 298ff.
30. J. D. Jackson, *Classical Electrodynamics*, New York: John Wiley, 1962, pp. 280–282.
31. M. Born and E. Wolf, *Principles of Optics*, 2nd ed., New York: MacMillan, 1964, pp. 414–418.
32. M. Françon, *Diffraction-Coherence in Optics*, Oxford: Pergamon Press, 1966, Chapter VI, Section 6.5.
33. P. Jacquinot and B. Roizen Dossier, "Apodization," in *Progress in Optics, Vol. III*, Emil Wolf, ed., Amsterdam, Netherlands: North Holland Publishing, 1964, pp. 30–186.
34. R. C. Hansen, "Aperture Theory," in *Microwave Scanning Antennas, Volume I: Apertures*, R. C. Hansen, ed., New York: Academic Press, 1964, pp. 47–101.
35. E. A. Wolff, *Antenna Analysis*, New York: John Wiley, 1966, pp. 109–135.
36. K. A. Karpov, *Tables of the Functions* $F(Z) = \int_0^Z e^{x^2}dx$ *in the Complex Domain*, New York: MacMillan, 1964.
37. W. J. Smith, *Modern Optical Engineering*, New York: McGraw-Hill, 1966, pp. 385–387.
38. E. C. Titchmarsh, *Introduction to the Theory of Fourier Integrals*, Oxford: Clarendon, 1948, pp. 61–66.
39. Jan Peřina, *Coherence of Light*, London: Van Nostrand Reinhold, 1972, pp. 32–42.
40. M. J. Beran and G. B. Parrent, *Theory of Partial Coherence*, Englewood Cliffs, New Jersey: Prentice-Hall, 1964, pp. 27–44.
41. H. E. Bennett and J. M. Bennett, "Precision Measurements in Thin Film Optics," in *Physics of Thin Films, Vol. 4*, G. Hass, ed., New York: Academic Press, 1967, pp. 1–96.
42. S. Tolansky, *Multiple-Beam Interferometry of Surfaces and Films*, New York: Dover Publications, 1970, Chapter IX, pp. 104–108.